# Isogeometric Boundary Element Analysis for Two-Dimensional Transient Heat Conduction Problems Based on the Radial Integration Method and the Application of Polynomial Chaos Expansion


Xinbo Jiang[1], Lian Huang[1], Yuanpeng Wang[2], Jinsheng Xuan[1] and Yanming Xu[1,3,*]

[1] Solux College of Architecture and Design, University of South China, West Changsheng Road, Hengyang, China

[2] Key Laboratory of *In-situ* Property-Improving Mining of Ministry of Education, Taiyuan University of Technology, Taiyuan, China

[3] Henan International Joint Laboratory of Structural Mechanics and Computational Simulation, College of Architecture and Civil Engineering, Huanghuai University, Zhumadian, China




**INFORMATION**

**Keywords:**
Isogeometric analysis
NURBS
boundary element method
polynomial chaos expansion
heat conduction
radial integration method

**DOI:** 10.23967/j.rimni.2026.10.77425

SCIPEDIA
Revista Internacional de Métodos Numéricos para Cálculo y Diseño en Ingeniería
RIMNI

# Isogeometric Boundary Element Analysis for Two-Dimensional Transient Heat Conduction Problems Based on the Radial Integration Method and the Application of Polynomial Chaos Expansion

**Xinbo Jiang[1], Lian Huang[1], Yuanpeng Wang[2], Jinsheng Xuan[1] and Yanming Xu[1,3,*]**

[1]Solux College of Architecture and Design, University of South China, West Changsheng Road, Hengyang, China

[2]Key Laboratory of *In-situ* Property-Improving Mining of Ministry of Education, Taiyuan University of Technology, Taiyuan, China

[3]Henan International Joint Laboratory of Structural Mechanics and Computational Simulation, College of Architecture and Civil Engineering, Huanghuai University, Zhumadian, China

## ABSTRACT

This study introduces a novel coupled computational framework that seamlessly fuses the Isogeometric Boundary Element Method (IGABEM) with the Polynomial Chaos Expansion (PCE) to address transient heat conduction problems under parametric uncertainty. The proposed approach transcends traditional numerical paradigms by constructing a unified formulation that intertwines geometric precision, computational efficiency, and probabilistic rigor. At the heart of the framework lie three tightly integrated representations. First, Non-Uniform Rational B-Splines (NURBS) basis functions serve a dual purpose—they simultaneously embody geometric modeling and field discretization. This duality allows for the direct transformation of Computer-Aided Design (CAD)-level geometric fidelity into the numerical domain, preserving intricate boundary characteristics while discretizing the governing boundary integral equations with remarkable exactness. Second, through the introduction of Bézier extraction, the computational overhead associated with NURBS basis evaluations is dramatically reduced. This operation reformulates complex NURBS structures into more manageable Bézier entities, unlocking substantial efficiency gains without compromising the inherent smoothness or precision of the geometric representation. Third, the framework incorporates Polynomial Chaos Expansion to systematically quantify and propagate uncertainties in material parameters. By coupling this stochastic representation with an advanced radial integration scheme, the method elegantly circumvents the need for conventional domain meshing while maintaining high accuracy in evaluating domain integrals. The result is a streamlined yet robust uncertainty quantification process embedded directly within the boundary element context. A series of numerical experiments corroborates the effectiveness of the proposed hybrid strategy. The findings reveal that the method not only preserves the celebrated advantages of IGABEM—such as geometric exactness and reduced-dimensional computation—but also extends its capability into the stochastic domain, enabling a comprehensive evaluation of how parameter uncertainties influence transient thermal responses. In essence, this integrated IGABEM–PCE framework bridges the gap between deterministic modeling and probabilistic analysis, yielding a unified, high-fidelity numerical tool. Its capacity to deliver both geometric accuracy and uncertainty quantification positions it as an indispensable technique for complex engineering scenarios, particularly in thermal management, energy conversion, and high-precision design systems, where reliability under uncertainty is paramount.

**OPEN ACCESS**

**Received:** 09/12/2025

**Accepted:** 19/01/2026

**Published:** 21/07/2026

**DOI**
10.23967/j.rimni.2026.10.77425

**Keywords:**
Isogeometric analysis
NURBS
boundary element method
polynomial chaos expansion
heat conduction
radial integration method

*Correspondence: Yanming Xu (xuyanming@ustc.edu). 

## 1 Introduction

Since Hughes et al. [1] first articulated its theoretical foundations in 2005, Isogeometric Analysis (IGA) has evolved from a conceptual innovation into one of the most influential paradigms in computational mechanics. Unlike the Finite Element Method (FEM) which relies on Lagrangian polynomial basis functions for spatial discretization, IGA diverges fundamentally by adopting spline-based representations, particularly Non-Uniform Rational B-Splines (NURBS), that are inherently consistent with Computer-Aided Design (CAD) geometry. This synthesis of geometry and analysis marks a profound shift: IGA erases the long-standing divide between modeling and simulation by employing the very same mathematical entities that define a structure's geometry to also approximate its physical fields.

The implications of this unification are far-reaching. By directly leveraging CAD-generated geometric data, IGA circumvents the cascade of approximation errors traditionally introduced through geometry reconstruction, mesh generation, and subsequent refinement stages that plague conventional FEM workflows. In doing so, it eliminates the artificial boundary between design and computation, forging a seamless pipeline from geometric conception to numerical realization.

Moreover, IGA's inherent high-order continuity—a natural consequence of its spline formulation—empowers it to capture complex physical behaviors with exceptional precision. Through k-refinement, an adaptive discretization strategy that simultaneously elevates polynomial order and enhances continuity, IGA attains unparalleled efficiency in resolving high-gradient fields and higher-order differential operators [2]. Consequently, it has demonstrated remarkable performance across a spectrum of challenging applications, spanning structural mechanics, fluid–structure interaction, electromagnetics, and thermal analysis [3–5].

To further streamline the practical deployment of IGA, researchers introduced the concept of Bézier extraction, a transformative technique that embeds the elegance of isogeometric formulations within existing finite element infrastructures—without necessitating radical architectural overhauls. The essence of this method lies in translating complex B-spline basis functions into an equivalent Bézier form through a well-defined algebraic mapping. This translation not only simplifies the computational process but also preserves the mathematical fidelity of the original formulation.

In effect, Bézier extraction bridges the gap between innovation and implementation. It retains IGA's superior accuracy and smoothness while greatly enhancing computational efficiency and code compatibility, thus enabling widespread adoption of isogeometric principles within conventional FEM environments. Through this synergy of mathematical rigor, geometric exactness, and algorithmic adaptability, IGA continues to redefine the frontiers of numerical simulation in modern engineering science.

Although Isogeometric Analysis (IGA) was originally conceived within the Finite Element Method (FEM) framework, its practical deployment across engineering disciplines soon revealed an intrinsic limitation—an underlying geometric incompatibility between the volumetric parameterization demanded by FEM and the boundary-representation (B-rep) paradigm that forms the foundation of modern Computer-Aided Design (CAD) systems. This incongruity poses a critical bottleneck: while CAD defines geometry primarily through boundary entities, FEM insists upon domain discretization, thereby introducing redundant volumetric meshing that undermines the geometric precision IGA was meant to preserve.

To reconcile this fundamental mismatch, researchers advanced a transformative idea, embedding the isogeometric philosophy directly into the Boundary Element Method (BEM). The resulting formulation, known as the Isogeometric Boundary Element Method (IGABEM), fuses the geometric exactness of CAD-based representations with the dimensional reduction inherent in boundary-only formulations. This synergy effectively bypasses the volumetric meshing dilemma, achieving both mathematical elegance and computational economy within a single unified framework.

In the context of heat conduction analysis, pioneering contributions from Fu et al. [6] and Mierzwiczak et al. [7] marked a defining moment in the evolution of IGABEM. Their work not only introduced the application of isogeometric principles to thermal problems but also proposed the innovative intensity factor method, a technique specifically designed to mitigate singularities in boundary integrals persistent challenge that has long impeded the numerical stability of traditional BEM formulations [8].

Building upon these foundational studies, Simpson et al. [9] further enriched the methodology by integrating Proper Orthogonal Decomposition (POD) techniques to construct reduced-order models for transient heat transfer problems. This extension significantly enhanced computational efficiency while maintaining fidelity to the full-scale thermodynamic behavior of the system.

The expansion of IGABEM's capabilities did not stop there. Lian et al. [10] subsequently broadened the scope of application by extending the framework to three-dimensional elastoplastic analyses, demonstrating the method's versatility and robustness in addressing complex, nonlinear material behaviors.

Collectively, these advancements signal a decisive maturation of IGABEM—from a theoretical adaptation of IGA principles into a powerful, boundary-focused computational paradigm capable of tackling a diverse array of engineering problems with geometric precision, reduced computational cost, and superior numerical stability.

In the realm of practical engineering analysis, it is seldom realistic to assume that material properties remain strictly deterministic. Parameters such as thermal conductivity, specific heat capacity, or even density are often imbued with inherent uncertainties, arising from manufacturing variations, environmental fluctuations, or incomplete experimental characterization. These uncertainties, though sometimes subtle, can profoundly influence the reliability and stability of numerical predictions—particularly in heat conduction and multiphysics simulations, where parameter sensitivity can cascade through coupled physical processes.

To rigorously quantify and propagate such uncertainties, the Polynomial Chaos Expansion (PCE) framework has emerged as one of the most powerful and elegant stochastic methods available. Recent comprehensive studies have further summarized the theoretical developments and efficient implementations of PCE for uncertainty quantification in complex engineering systems [11,12]. Unlike conventional Monte Carlo approaches that rely on exhaustive sampling, PCE achieves remarkable computational efficiency by representing random input variables through a series expansion of orthogonal polynomials defined over the probability space of the uncertain parameters. Each polynomial basis term captures a distinct mode of stochastic variation, allowing the response quantity—such as temperature or flux—to be expressed as a smooth functional mapping of the random input space.

This formulation not only facilitates rapid uncertainty propagation but also provides a mathematically consistent foundation for global sensitivity analysis, enabling researchers to discern which uncertain parameters exert dominant influence on the overall system behavior. Consequently, PCE stands as a cornerstone technique in uncertainty quantification, combining analytical clarity with

numerical robustness to transform probabilistic modeling from an abstract concept into a practical, computation-ready methodology for complex engineering systems.

The integration of Polynomial Chaos Expansion (PCE) with the Isogeometric Boundary Element Method (IGABEM) represents a profound advancement in the field of computational uncertainty quantification [13]. Relative to traditional stochastic finite element methods, it avoids the cumbersome generation of volume meshes and inherently benefits from geometric exactness through isogeometric descriptions; compared to stochastic boundary element methods or collocation methods that still require internal meshes, it completely eliminates domain discretization via the radial integration technique, maintaining a pure boundary-reduction characteristic; and in contrast to general surrogate model approaches, it offers a high-fidelity deterministic solver based on the isogeometric boundary element method, thereby ensuring an accuracy foundation for the coefficients of the PCE.

Unlike the Finite Element Method (FEM), the Boundary Element Method (BEM) demands only boundary discretization [14–18]. This inherent reduction in dimensionality not only mitigates the computational overhead associated with volumetric meshing but also aligns naturally with CAD's boundary representation (B-rep) architecture. The isogeometric extension of BEM thus forms a methodologically elegant bridge between numerical simulation and geometric modeling, allowing direct utilization of CAD-derived NURBS surfaces as both geometric and analytical constructs.

Since its inception, IGABEM has demonstrated a remarkable spectrum of applicability. Early studies established its viability in potential problem analysis [19,20] and elasticity modeling [21], laying the foundation for its rapid expansion into diverse scientific and engineering domains. It has since achieved notable success in heat conduction studies [22], linear elasticity problems [23,24], and fracture mechanics investigations [25], where boundary singularities and stress concentration phenomena demand exceptional numerical precision. Moreover, its efficacy extends into electromagnetic computations [26], acoustic propagation analyses [27–31], and structural optimization design [32–36], where the combination of exact boundary geometry and reduced system dimensionality yields superior computational performance.

Collectively, these advancements underscore IGABEM's unparalleled versatility in addressing complex, large-scale, and geometrically intricate engineering problems. Its boundary-only formulation not only ensures computational economy but also maintains CAD-consistent geometric integrity, an attribute critical for applications involving infinite or semi-infinite domains, moving interfaces, or localized stress concentrations. When further augmented with PCE-based stochastic analysis, the method evolves into a comprehensive computational paradigm—one capable of delivering deterministic accuracy and probabilistic insight within a single, coherent framework.

This study presents an extended formulation of the Isogeometric Boundary Element Method (IGABEM) tailored for the numerical analysis of heat conduction phenomena, further enhanced through the integration of Polynomial Chaos Expansion (PCE) to achieve comprehensive uncertainty quantification [37]. The proposed framework unites geometric precision, computational efficiency, and probabilistic analysis into a single, cohesive methodology. Its relevance extends across a wide spectrum of engineering disciplines—most notably energy conversion systems, electronic thermal management, aerospace thermal protection, and other domains where accurate prediction of heat transfer under uncertainty is vital to design reliability and system optimization.

A persistent challenge in applying boundary-based formulations to heat conduction problems lies in the evaluation of domain integrals that inevitably arise during computation. To address this issue, the present work adopts the radial integration method introduced by Liu et al. [38], which elegantly transforms domain integrals into boundary integrals, thus preserving the inherent boundary-only

nature of IGABEM. This approach markedly enhances computational efficiency while maintaining numerical stability, particularly for cases involving non-homogeneous materials or spatially varying coefficients.

The investigation encompasses a comprehensive suite of thermal simulations, examining both steady-state and transient heat conduction under a range of constant and variable coefficient conditions. Through these scenarios, the study rigorously evaluates the robustness of the proposed framework in capturing the intricate temporal and spatial evolution of temperature fields, as well as its sensitivity to material and boundary uncertainties represented through PCE expansions [39].

The primary contributions of this work are summarized as follows:

(i) the integration of the radial integration method into IGABEM for transient heat conduction.

(ii) the introduction of PCE into a boundary-only isogeometric framework for uncertainty quantification.

(iii) the resulting unified framework that preserves CAD-consistent geometry while enabling efficient stochastic analysis.

The organizational structure of the remaining sections is arranged as follows: Section 2 establishes the mathematical foundations underpinning the method, including an exposition of B-spline and NURBS basis functions and a detailed account of the PCE framework for stochastic representation. Section 3 elucidates the implementation principles of Bézier extraction, a technique employed to simplify NURBS computations and facilitate integration within standard numerical infrastructures. Section 4 formulates the boundary integral equation for heat conduction, providing a meticulous derivation of the temporal discretization and time-marching scheme used for transient analysis. Section 5 presents two representative numerical examples that validate the proposed method's accuracy, stability, and convergence properties, highlighting its capacity to reconcile geometric fidelity with uncertainty propagation. Finally, Section 6 synthesizes the principal findings, emphasizing the method's theoretical contributions and practical significance, and outlines promising directions for future research, including potential extensions to multi-physics coupling and high-dimensional stochastic modeling.

## 2 PCE Method

### *2.1 PCE Method and Legendre Orthogonal Polynomials*

In the context of stochastic system analysis, the probabilistic behavior of a system can be rigorously represented through a hierarchy of orthogonal polynomial bases, each corresponding to distinct modes of random variation within the underlying uncertainty space. By invoking the Polynomial Chaos Expansion (PCE) framework, these basis functions provide a mean-square convergent approximation of stochastic processes, ensuring that the series representation asymptotically captures the full statistical structure of the system response as the polynomial order increases. Recently, physics-informed polynomial chaos expansion frameworks have been proposed by incorporating governing equation constraints into the surrogate construction, which can further improve prediction accuracy for complex PDE-governed systems [40].

Formally, the stochastic formulation is established upon a probability space defined by the triple $(\Omega_p, B, P)$, where $\Omega_p$ denotes the sample space containing all possible realizations $\omega_p$ of the random phenomenon, B represents the complete $\sigma$-algebra constructed over the measurable subsets of $\Omega_p$, and P corresponds to the probability measure that quantifies the likelihood of each measurable event. Within this probabilistic framework, any second-order integrable function $T(\boldsymbol{\xi})$ defined over the random vector $\xi = (\xi_1, \xi_2, ..., \xi_n)$ and possessing finite second-order moments—that is, a well-defined

expectation and variance—can be faithfully expressed through a polynomial chaos representation, provided that the random variables $\xi_i$ are mutually independent and share identical prior probability distributions.

Assuming each stochastic component $\xi_i$ takes values within the bounded interval $[-1, 1]$, the corresponding system response function $T(\boldsymbol{\xi})$ may be expanded as a finite or infinite orthogonal polynomial series, written formally as:

$$T(\xi) \approx \sum_{i=0}^{P} c_i \Phi_i(\xi) \tag{1}$$

where $c_i$ denotes the deterministic coefficients (or chaos modes) that encode the projection of the system response onto the polynomial basis, and $\Phi_i(\boldsymbol{\xi})$ represents the multivariate orthogonal polynomial functions defined with respect to the probability measure P. Each term in this expansion contributes to the hierarchical decomposition of the stochastic field, with higher-order polynomials capturing progressively more intricate interactions among the underlying random inputs.

The coefficients are typically calculated through the following formulation:

$$P = C_{n+p}^{p} \tag{2}$$

The standard Legendre polynomials $P_n(\xi)$ are defined on the interval $\xi \in [-1, 1]$ and satisfy the following orthogonality condition:

$$\int_{-1}^{1} P_m(\xi) P_n(\xi) d\xi = \frac{2}{2n+1} \delta_{mn} \tag{3}$$

where $\delta_{mn}$ denotes the Kronecker delta function, taking the value 1 when m equals n and 0 otherwise.

Legendre polynomials can be derived as solutions to the following two random variables second-order ordinary differential equation:

$$\frac{d}{d\xi}\left\{(1-\xi^2)\frac{d}{d\xi}P_k\{\xi\}\right\} + k(k+1)P_k\{\xi\} = 0, k = 0, 1, 2, \ldots \tag{4}$$

Through this construction, PCE transforms the abstract probabilistic characterization of uncertainty into an explicit functional form, allowing the system response to be quantified, propagated, and analyzed within a deterministic computational framework. The resulting representation provides not only a mathematically rigorous description of randomness but also a computationally tractable pathway for performing uncertainty quantification and sensitivity analysis in complex engineering systems.

Table 1 presents the explicit expressions of the first seven orders of Legendre polynomials, which form a complete orthogonal function system over the interval $[-1, 1]$. These polynomials obey a well-defined recurrence relation expressed mathematically as follows:

**Table 1:** First seven one-dimensional Legendre polynomials

| k | Legendre polynomials $\mathbf{P_k(\xi)}$ |
|---|---|
| 0 | 1 |
| 1 | $\xi$ |

(Continued)

**Table 1 (continued)**

| k | Legendre polynomials $\mathbf{P_k(\xi)}$ |
|---|---|
| 2 | $\frac{1}{2}\left(3\xi^2-1\right)$ |
| 3 | $\frac{1}{2}\left(5\xi^3-3\xi\right)$ |
| 4 | $\frac{1}{8}\left(35\xi^5-30\xi^3+3\xi\right)$ |
| 5 | $\frac{1}{8}\left(63\xi^5-70\xi^3+15\xi\right)$ |
| 6 | $\frac{1}{16}\left(231\xi^6-315\xi^4+105\xi^2-5\right)$ |
| 7 | $\frac{1}{16}\left(429\xi^7-693\xi^5+325\xi^3-35\xi\right)$ |

For a uniformly distributed random variable $X \sim U(a, b)$, the affine transformation $\xi = \frac{2X-(a+b)}{b-a}$ serves as a pivotal mapping that linearly transposes the stochastic domain from its native support $[a, b]$ to the standardized interval $\xi \in [-1, 1]$. This transformation establishes a direct correspondence between the physical random variable X and its normalized probabilistic counterpart $\xi$, thereby aligning the random input with the orthogonality domain of the Legendre polynomial basis.

Through this normalization process, the stochastic representation of X becomes dimensionless and distributionally consistent, allowing the Legendre polynomial system—which is intrinsically orthogonal over $[-1, 1]$—to be employed for constructing Polynomial Chaos Expansions (PCE). The transformation thus ensures that the probability density function (PDF) of $\xi$ remains uniform, preserving the statistical equivalence between X and $\xi$ while simplifying the subsequent analytical treatment of uncertainty propagation.

In essence, this mapping forms a crucial bridge between the physical parameter space and the canonical polynomial chaos space, facilitating the projection of stochastic responses onto a mathematically orthogonal basis. The result is a computationally elegant framework where random variables, once rescaled into the standardized domain, can be expanded precisely through Legendre polynomials, yielding both analytical tractability and numerical efficiency in uncertainty quantification.

### *2.2 Evaluation of Polynomial Chaos Expansion*

In practical numerical computations, discrepancies inevitably arise between the predicted model responses T and the theoretical reference values $\hat{T}$. To rigorously assess the predictive accuracy of the proposed surrogate model, this study adopts the Coefficient of Variation of the Root Mean Square Error (CV(RMSE)) as a quantitative evaluation metric. This indicator serves not only as a direct measure of model fidelity but also as an effective diagnostic tool for verifying the convergence characteristics of the Polynomial Chaos Expansion (PCE) by examining the statistical distribution of output responses.

The CV(RMSE) is formally defined as:

$$\mathrm{CV(RMSE)} = \frac{\sqrt{\frac{\sum_{i=1}^{n}(T_i - \hat{T}_i)^2}{n}}}{\frac{\sum_{i=1}^{n} T_i}{n}} \tag{5}$$

In this formulation, n denotes the total number of sampling points, $T_i$ represents the original outputs obtained from the high-fidelity numerical model, and $\hat{T}_i$ corresponds to the temperature responses predicted by the PCE-based surrogate model. By normalizing the root-mean-square error with respect to the mean output, this measure provides a dimensionless and scale-independent criterion for evaluating model accuracy, thereby ensuring consistency across different magnitudes of physical quantities.

A model is considered to exhibit satisfactory predictive performance when the normalized root-mean-square error falls below a 5% threshold. Under such conditions, the PCE surrogate demonstrates strong agreement with the reference model, confirming both its convergence behavior and reliability in capturing stochastic system responses under parametric uncertainty.

## 3 NURBS

NURBS are constructed upon the mathematical foundation of B-splines, characterized by a set of control points, a knot vector, and corresponding basis functions. The basis functions, denoted as $U = \{u_1, u_2, \ldots, u_m\}$, are defined piecewise over a non-decreasing real sequence, where U represents the knot vector, and each individual knot $u_i$ specifies a distinct parameter value within that sequence. The B-spline basis functions are formulated recursively according to the following definition:

Zero-degree basis function ($p = 0$)

$$N_{i,0}(u) = \begin{cases} 1 & \text{if } u_i \le u < u_{i+1} \\ 0 & \text{other} \end{cases} \tag{6}$$

Higher-order basis functions ($p > 0$)

$$N_{i,p}(u) = \frac{u - u_i}{u_{i+p} - u_i} N_{i,p-1}(u) + \frac{u_{i+p+1} - u}{u_{i+p+1} - u_{i+1}} N_{i+1,p-1}(u) \tag{7}$$

where p specifies the polynomial degree of the B-spline basis functions and n corresponds to the number of shape functions in the discretization.

The derivatives of the basis functions can be obtained as follows:

$$\dot{N}_{i,p} = \frac{p}{u_{i+p} - u_i} N_{i,p-1} - \frac{p}{u_{i+p+1} - u_{i+1}} N_{i+1,p-1}\,(u) \tag{8}$$

The geometric configuration of a B-spline curve is determined by the linear superposition of NURBS weighting functions with associated control points.

$$C(u) = \sum_{i=0}^{n} N_{i,p}(u) P_i \tag{9}$$

where $P_i$ represents the control point coordinates in Cartesian space.

The purely polynomial form of the B-spline basis functions, $N_{i,p}(u)$, inherently constrains their ability to exactly represent conic sections, such as circular or elliptical arcs. To overcome this

limitation, weights $w_i$ are introduced, enabling the construction of rational basis functions through a normalization process. This refinement yields the mathematical formulation of NURBS curves, expressed as follows:

$$C(u) = \sum_{i=0}^{n} R_{i,p}(u)P_i = \frac{\sum_{i=0}^{n} w_i N_{i,p}(u)P_i}{\sum_{i=0}^{n} w_i N_{i,p}(u)} \tag{10}$$

where $R_{i,p}(u) = \dfrac{w_i N_{i,p}(u)}{\sum_{j=0}^{n} w_j N_{j,p}(u)}$ is the NURBS basis function.

Owing to their rational formulation, in which the B-spline basis functions are combined with corresponding weight factors ω, NURBS basis functions possess the capability to accurately represent conic sections as well as geometrically complex curves.

In the isogeometric boundary element method, both the geometry and field variables are represented by NURBS basis functions, and the approximation accuracy depends on the density of control points. Increasing the number of control points improves the geometric representation and the accuracy of the unknown fields; however, once the geometry is represented with sufficient accuracy, further refinement leads to diminishing gains in numerical accuracy.

## 4 Bézier Extraction

In the Isogeometric Boundary Element Method (IGABEM), the Bézier extraction technique is utilized to significantly enhance computational efficiency. The fundamental idea of this approach lies in constructing a linear transformation operator that establishes a correspondence between the Bernstein polynomial basis functions of local Bézier elements and the global B-spline basis functions. This relationship is realized through a specialized transformation matrix, commonly referred to as the extraction operator. In particular, performing the transpose operation of this extraction operator enables the conversion of global B-spline control points into their corresponding Bézier curve control points. For detailed formulations and algorithmic derivations, readers are referred to references [41,42].

During the Bézier decomposition process, operations must be iteratively performed on all interior knots until the multiplicity of each knot equals the degree p of the curve. In practical implementation, when a new knot $u^*$ is inserted immediately after the $k$-th knot in the original knot vector $\Xi = u_1, u_2, \ldots, u_{n+p+1}$, the updated knot vector becomes $\Xi^{`} = u_1, u_2, \ldots, u_k, u^*, u_{k+1}, \ldots, u_{n+p+1}$, where the insertion position must satisfy the condition $k > p$. The knot insertion operation induces a reconstruction of the basis functions and necessitates the computation of a new set of control points. By analyzing the geometric relationships between the original and modified curve representations, a direct mapping relation can be established to link the initial control points P with the transformed control points Q. This relationship is mathematically expressed as follows:

$$Q_i = \begin{cases} P_1, & i = 1 \\ \alpha_i P_i + (1-\alpha_i)P_{i-1}, & 0 < i < m \\ P_n, & i = m \end{cases} \tag{11}$$

where $m = n + 1$, and the parameter $\alpha_i$ is computed via the relation:

$$\alpha_i = \begin{cases} 1, & i \le k - p; \\ \dfrac{u^* - u_i}{u_{i+p} - u_i}, & k - p + 1 \le i \le k \\ 0, & i \ge k + 1 \end{cases} \tag{12}$$

Following the knot insertion operations, the control points are correspondingly updated to reflect the modified curve geometry. Let $\{u_1^*, u_2^*, \ldots, u_m^*\}$ denote the complete set of knots required to perform the Bézier decomposition of the original B-spline. For each newly inserted knot $u^*(j = 1, 2 \ldots, m)$, the parameter $\alpha_i^j$is defined in accordance with Eq. (9) for $i = 1, 2 \ldots, n + j$, where $a_i^j$ represents the $\alpha$-value associated with the *i*-th position. Consequently, the corresponding transformation matrix C can be formulated as follows:

$$C_j = \begin{bmatrix} \alpha_1 & 1-\alpha_2 & 0 & \cdots & & & 0 \\ 0 & \alpha_2 & 1-\alpha_3 & 0 & \cdots & & 0 \\ 0 & 0 & \alpha_3 & 1-\alpha_4 & 0 & \cdots & 0 \\ \vdots & & & & & & \\ 0 & \cdots & & & 0 & \alpha_{n+j-1} & 1-\alpha_{n+j} \end{bmatrix} \tag{13}$$

The new control points are obtained through the following formula:

$$Q = C_m^T \cdots C_1^T P \tag{14}$$

The transformation can be expressed in matrix form as:

$$Q = C^T P \tag{15}$$

A B-spline curve defined on the knot vector $\{0, 0, 0, 0.25, 0.5, 0.75, 1, 1, 1\}$ can be decomposed through the Bézier extraction process. This procedure begins by inserting additional knots $\{0.25, 0.25, 0.5, 0.5, 0.75, 0.75\}$ into the existing knot vector, thereby increasing the multiplicity of each interior knot to match the degree of the curve. Following this operation, the original B-spline curve is transformed into a composite representation composed of multiple Bézier segments, without inducing any alteration to its geometric configuration. The resulting curve can thus be expressed entirely in terms of standard Bézier basis functions, while preserving identical geometric fidelity to the original B-spline form. The mathematical formulation of the B-spline curve represented via Bézier basis functions is expressed as follows:

$$C(u) = \sum_{i=1}^{n} N_{i,p} P_i = \sum_{i=1}^{m} B_{i,n} Q_i \tag{16}$$

Substituting Eq. (15) into Eq. (16) yields:

$$C(u) = Q^T B(u) = \left(C^T P\right)^T B(u) = P^T C B(u) = P^T N(u) \tag{17}$$

Since P is arbitrary, we obtain the following fundamental equation:

$$N(u) = CB(u) \tag{18}$$

The extraction operator matrix C is completely determined by the knot vector and can be expressed as a product function of the corresponding parametric intervals. Its construction remains independent of both the control points and the basis functions, thereby allowing for a direct generalization to NURBS conversion computations. By defining the weights in the form of a diagonal matrix, we have:

$$W = \begin{bmatrix} \omega_1 & & \\ & \ddots & \\ & & \omega_n \end{bmatrix} \tag{19}$$

Substituting Eqs. (18) and (19) into Eq. (10) yields the NURBS curve expressed in terms of Bernstein basis functions:

$$\mathrm{T}(\mathrm{u}) = \frac{1}{\omega^{\mathrm{T}}\mathrm{CB}(\mathrm{u})}\mathrm{P}^{\mathrm{T}}\mathrm{WCB}(\mathrm{u}) \tag{20}$$

Let $\omega_b = C^T\omega$, and define Wb as the diagonal matrix:

$$\mathrm{W}^{\mathrm{b}} = \begin{bmatrix} \mathrm{w}_1^{\mathrm{b}} & & & \\ & \mathrm{w}_2^{\mathrm{b}} & & \\ & & \ddots & \\ & & & \mathrm{w}_{\mathrm{n+m}}^{\mathrm{b}} \end{bmatrix} \tag{21}$$

Eq. (15) can be expressed as:

$$\mathrm{T}(\mathrm{u}) = \frac{1}{(\omega^{\mathrm{b}})^{\mathrm{T}}\mathrm{B}(\mathrm{u})}\mathrm{P}^{\mathrm{T}}\mathrm{WCB}(\mathrm{u}) \tag{22}$$

The expression for Bézier control points can be derived using homogeneous coordinate representation:

$$\mathrm{P}^{\mathrm{b}} = \left(\mathrm{W}^{\mathrm{b}}\right)^{-1}\mathrm{C}^{\mathrm{T}}\mathrm{WP} \tag{23}$$

Multiplying both sides by $W^b$ yields the homogeneous coordinate representation of the Bézier control points:

$$\mathrm{W}^{\mathrm{b}}\mathrm{P}^{\mathrm{b}} = \mathrm{C}^{\mathrm{T}}\mathrm{WP} \tag{24}$$

Upon completing the Bézier operations, the weight factors $w^b$ and control points $P^b$ are determined, yielding the final Bézier representation of the NURBS curve:

$$\mathrm{T}(\mathrm{u}) = \frac{1}{\mathrm{W}^{\mathrm{b}}(\mathrm{u})}\left(\mathrm{W}^{\mathrm{b}}\mathrm{P}^{\mathrm{b}}\right)^{\mathrm{T}}\mathrm{B}(\mathrm{u}) = \sum\nolimits_{\mathrm{i}=1}^{\mathrm{n+m}}\frac{\mathrm{P}_{\mathrm{i}}^{\mathrm{b}}\omega_{\mathrm{i}}^{\mathrm{b}}\mathrm{B}_{\mathrm{i}}(\mathrm{u})}{\mathrm{W}^{\mathrm{b}}(\mathrm{u})} \tag{25}$$

Finally, the NURBS can be equivalently represented by a series of $C^0$ Bézier elements.

Obviously, the present IGABEM framework integrates CAD-exact NURBS geometry via IGA and leverages Bézier extraction for efficiency. It retains the dimensional-reduction advantage of BEM while eliminating geometry approximation and mesh generation, resulting in a streamlined and geometrically faithful design-to-simulation workflow.

## 5 Governing Equations

The governing equation describing transient heat conduction in an isotropic medium with constant material properties and internal heat generation is formulated as follows:

$$k\nabla^2\mathrm{T}(x,t) + b(x,t) = \rho c_p\frac{\partial \mathrm{T}(x,t)}{\partial t}(t \geq t_0, x \in \Omega) \tag{26}$$

here, $T(x,t)$ denotes the temperature field at spatial position x and time t; k represents the thermal conductivity; $b(x,t)$ corresponds to the heat source term defined over the domain; $\rho$ is the material density; $c_p$ the specific heat capacity; and $t_0$ denotes the initial time.

Considering the following boundary conditions:

$$\mathrm{T}(\mathbf{x},\mathrm{t}) = \overline{\mathrm{T}}(\mathbf{x},\mathrm{t}) \ (\mathrm{t} \geq \mathrm{t}_0, \mathbf{x} \in \Gamma_1) \tag{27}$$

$$\mathrm{q}(\mathbf{x},\mathrm{t}) = -k\frac{\partial T(\mathbf{x},\mathrm{t})}{\partial \boldsymbol{n}(\mathbf{x})} = \overline{q}(\mathbf{x},\mathrm{t}) \ (\mathrm{t} \geq \mathrm{t}_0, \mathbf{x} \in \Gamma_2) \tag{28}$$

In this context, q denotes the heat flux, $\overline{\mathrm{T}}$ represents the prescribed temperature on the boundary, and $\overline{\mathrm{q}}$ specifies the prescribed boundary heat flux. The overall boundary of the computational domain, $\Gamma$ is composed of two distinct segments, such that $\Gamma = \Gamma_1 + \Gamma_2$. Here, $n$ designates the unit outward normal vector defined along the boundary $\Gamma$.

with the initial condition:

$$\mathrm{T}(\mathbf{x},\mathrm{t}_0) = \mathrm{T}_0(\mathbf{x}) \ (\mathbf{x} \in \Omega) \tag{29}$$

$$\mathrm{q}(\mathbf{x},\mathrm{t}_0) = \mathrm{q}_0(\mathbf{x}) \ (\mathbf{x} \in \Gamma) \tag{30}$$

### *5.1 Boundary Element Method for Transient Temperature Fields*

Applying the weighted residual method with integration by parts to Eq. (21) yields the boundary domain integral formulation:

$$\begin{aligned} \mathrm{c}(\mathrm{p})\,\tilde{\mathrm{T}}(\mathrm{p},\mathrm{t}) = & -\int_\Gamma \mathrm{q}^*(\mathrm{Q},\mathrm{p})\,\tilde{\mathrm{T}}(\mathrm{Q},\mathrm{t})\,\mathrm{d}\Gamma(\mathrm{Q}) - \int_\Gamma \mathrm{u}^*(\mathrm{Q},\mathrm{p})\,\mathrm{q}(\mathrm{Q},\mathrm{t})\,\mathrm{d}\Gamma(Q) \\ & + \int_\Omega \mathrm{u}^*(\mathrm{q},\mathrm{p})\,\mathrm{b}(\mathrm{q},\mathrm{t})\,\mathrm{d}\Omega(q) - \int_\Omega \mathrm{u}^*(\mathrm{q},\mathrm{p})\,\tilde{\rho}\,\tilde{\mathrm{T}}(\mathrm{q},\mathrm{t})\,\mathrm{d}\Omega(\mathrm{q}). \end{aligned} \tag{31}$$

The coefficient c takes the value of 1 when the source point $p$lies inside the domain $\Omega$, and 0.5 when it is located on a smooth boundary. The term $\tilde{\mathrm{T}} = \mathrm{KT}$ denotes the normalized temperature, while $\tilde{\rho} = \rho \mathrm{c}_\mathrm{p}/\mathrm{k}$ represents the reciprocal of the thermal diffusivity. The fundamental solution $\mathrm{u}^*$ and its derivative $\mathrm{q}^*$ are defined as follows:

$$\begin{cases} \mathrm{u}^* = \dfrac{1}{2\pi}\ln\left(\dfrac{1}{\mathrm{r}}\right) \\ \mathrm{q}^* = \dfrac{\partial \mathrm{u}^*}{\partial \mathbf{n}} = \dfrac{-1}{2\pi \mathrm{r}}\dfrac{\partial \mathrm{r}}{\partial \mathbf{n}} \end{cases} \tag{32}$$

In this project, we exclude internal heat sources, leading to the following modified form of Eq. (26):

$$\mathrm{c}(\mathrm{p})\,\tilde{\mathrm{T}}(\mathrm{p},\mathrm{t}) = -\int_\Gamma \mathrm{q}^*(\mathrm{Q},\mathrm{p})\,\tilde{\mathrm{T}}(\mathrm{Q},\mathrm{t})\,\mathrm{d}\Gamma(\mathrm{Q}) - \int_\Gamma \mathrm{u}^*(\mathrm{Q},\mathrm{p})\,\mathrm{q}(\mathrm{Q},\mathrm{t})\,\mathrm{d}\Gamma(\mathrm{Q}) - \int_\Omega \mathrm{u}^*(\mathrm{q},\mathrm{p})\,\tilde{\rho}\dot{\tilde{\mathrm{T}}}(\mathrm{q},\mathrm{t})\,\mathrm{d}\Omega(\mathrm{q}) \tag{33}$$

It is observed that the final term in Eq. (28) represents a domain integral, which can be transformed into an equivalent boundary integral through application of the radial integration method, thereby preserving the dimensional reduction advantage that is intrinsic to IGABEM.

The unknown temperature gradient, denoted as $\dot{\tilde{\mathrm{T}}}$, is initially approximated through interpolation, wherein radial basis functions (RBFs) are commonly adopted as the interpolation framework.

By selecting a set of appropriate collocation points for the interpolation process, an approximate expression of the temperature gradient variable can then be formulated as follows:

$$\dot{\tilde{T}}(q,t) = \sum_{i=1}^{N} \gamma_i f_i(r(q)) \tag{34}$$

here, N denotes the total number of collocation points, $\gamma_i$ represents the undetermined coefficient associated with the *i*-th collocation point, and $f_i(r)$ designates the corresponding radial basis function. The variable $r = |x^q - x^i|$ defines the inter-nodal distance between the observation point $x^q$ and the collocation point $x^i$, where $x^i$ explicitly specifies the spatial coordinates of the *i*-th collocation point.

It should be emphasized that the collocation points can be selected from either the boundary or the interior of the domain. Empirical evidence indicates that a combined selection of boundary and interior points substantially enhances the accuracy of the resulting approximate solution. Moreover, the inclusion of quadratic polynomial terms within the radial basis functions further improves the approximation quality, yielding a more stable and precise numerical representation.

$$\dot{\tilde{T}}(q,t) = \sum\nolimits_{i=1}^{N} \gamma_i f_i(r(q)) + \beta_0 + \sum\nolimits_{i=1}^{2} \beta_i x_i + \sum\nolimits_{i=1}^{2} \sum\nolimits_{j=i}^{2} \beta_{ij} x_i x_j \tag{35}$$

where $x^i$ and $x^j$ represent Cartesian coordinate components of point x, subject to the following conditions:

$$\begin{cases} \sum_{i=1}^{N} \gamma_i = 0 \\ \sum_{i=1}^{N} \gamma_i x_1^i = \sum_{i=1}^{N} \gamma_i x_2^i = 0 \\ \sum_{i=1}^{N} \gamma_i x_1^i x_1^i = \sum_{i=1}^{N} \gamma_i x_2^i x_2^i = \sum_{i=1}^{N} \gamma_i x_1^i x_2^i = 0 \end{cases} \tag{36}$$

The determination of the coefficients γ and β in Eq. (35) is of critical importance. Although these coefficients cannot be explicitly represented, their implicit formulations can be derived through appropriate variable substitution. By substituting the collocation points x into Eq. (35) and reformulating the resulting expressions in matrix–vector form, the following relationship is obtained:

$$fv = \dot{\tilde{T}} \tag{37}$$

where

$$\mathbf{f} = \begin{bmatrix} f^{11} & f^{12} & \cdots & f^{1N} & 1 & x_1^1 & x_2^1 & x_1^1x_2^1 & x_1^1x_1^1 & x_2^1x_2^1 \\ f^{21} & f^{22} & \cdots & f^{2N} & 1 & x_1^2 & x_2^2 & x_1^2x_2^2 & x_1^2x_1^2 & x_2^2x_2^2 \\ \vdots & \vdots & & \vdots & \vdots & \vdots & \vdots & \vdots & \vdots & \vdots \\ f^{N1} & f^{N2} & \cdots & f^{NN} & 1 & x_1^N & x_2^N & x_1^Nx_2^N & x_1^Nx_1^N & x_2^Nx_2^N \\ 1 & 1 & \cdots & 1 & 0 & 0 & 0 & 0 & 0 & 0 \\ x_1^1 & x_1^2 & \cdots & x_1^N & 0 & 0 & 0 & 0 & 0 & 0 \\ x_2^1 & x_2^2 & \cdots & x_2^N & 0 & 0 & 0 & 0 & 0 & 0 \\ x_1^1x_2^1 & x_1^2x_2^2 & \cdots & x_1^Nx_2^N & 0 & 0 & 0 & 0 & 0 & 0 \\ x_1^1x_1^1 & x_1^1x_2^1 & \cdots & x_1^Nx_1^N & 0 & 0 & 0 & 0 & 0 & 0 \\ x_2^1x_2^1 & x_2^2x_2^2 & \cdots & x_2^Nx_2^N & 0 & 0 & 0 & 0 & 0 & 0 \end{bmatrix} \tag{38}$$

$$v = \begin{bmatrix} \gamma_1 & \gamma_2 & \cdots & \gamma_N & \beta_0 & \beta_1 & \beta_2 & \beta_{11} & \beta_{12} & \beta_{22} \end{bmatrix}^T \tag{39}$$

$$\dot{\tilde{T}} = \begin{bmatrix} \dot{\tilde{T}}_1 & \dot{\tilde{T}}_2 & \cdots & \dot{\tilde{T}}_N & 0 & \cdots & 0 \end{bmatrix}^T \tag{40}$$

In Eq. (38), $f^{ij} = f_j(r)$ with $r = |x_i - x_j|$, and $\dot{\tilde{T}}$ denotes the temperature derivative at the $i$-th collocation point.

$$v = f^{-1}\dot{\tilde{T}} \tag{41}$$

Substituting Eq. (36) into the final term on the right-hand side of Eq. (33) and applying the radial integration method yields:

$$\int_\Omega u^*(q,p)\,\tilde{\rho}\dot{\tilde{T}}(q,t)\,d\Omega(q) = I_0 + I_1 + I_2 \tag{42}$$

where

$$I_0 = \sum_{i=1}^{N}\gamma_i \int_\Gamma \frac{A_i(Q,p)}{r(Q,p)}\frac{\partial r}{\partial n}d\Gamma(Q)$$

$$I_1 = \sum_{i=1}^{2}\beta_i \int_\Gamma \frac{r_{,k}\tilde{A}^1(Q,p)}{r(Q,p)}\frac{\partial r}{\partial n}d\Gamma(Q)$$

$$I_2 = \left(\beta_0 + \sum_{i=1}^{2}\beta_i x_i\right)\int_\Gamma \frac{A_0(Q,p)}{r(Q,p)}\frac{\partial r}{\partial n}d\Gamma(Q) \tag{43}$$

and

$$\begin{cases} A_i(x,y) = \int_0^{r(Q,p)} u^*(q,p)\,\tilde{\rho}f_i(r)\,r(q,p)\,dr(q) \\ \tilde{A}^1(x,y) = \int_0^{r(Q,p)} u^*(q,p)\,\tilde{\rho}r^2(q,p)\,dr(q) \\ A_0(x,y) = \int_0^{r(Q,p)} u^*(q,p)\,\tilde{\rho}r(q,p)\,dr(q) \end{cases} \tag{44}$$

Eq. (42) successfully achieves the domain-to-boundary transformation based on the fundamental solution, with detailed derivation procedures provided in Reference [43].

It should be noted that the coefficients appearing in Eq. (43) are unknown quantities, thereby precluding the direct computation of $I_0$, $I_1$, and $I_2$ through conventional boundary integration. In practical implementation, however, the explicit numerical evaluation of these coefficients is unnecessary.

When the source point $p$ coincides with the $i$-th collocation point, the terms $I_0$, $I_1$, and $I_2$ can be reformulated as vector inner products, leading to the following combined expression:

$$\int_\Omega u^*(q,p)\,\tilde{\rho}\dot{\tilde{T}}(q,t)\,d\Omega(q) = F^i v \tag{45}$$

The vector F encompasses the results of the boundary integral obtained from Eq. (42). By substituting Eq. (41) into Eq. (45), the following formulation is obtained:

$$\int_\Omega u^*(q,p)\,\tilde{\rho}\dot{\tilde{T}}(q,t)\,d\Omega(q) = F^i f^{-1}\dot{\tilde{T}} = C^i\dot{\tilde{T}} \tag{46}$$

By selecting the collocation points p and substituting them into Eq. (46), a matrix–vector product formulation is established through the simultaneous equations corresponding to all collocation points. In this formulation, the coefficient matrix satisfies the relation $C = Ff^{-1}$.

### *5.2 Discretization of the Boundary Integral Equation*

First, the boundary is discretized into $N_e$ non-overlapping NURBS elements:

$$\Gamma = \bigcup_{e=1}^{Ne}, \Gamma_i \bigcap \Gamma_j = \mathbf{0}, i \neq j \tag{47}$$

Within any NURBS element e, the unknown variables can be approximated using NURBS basis functions through the following representation:

$$\begin{cases} \tilde{T}(\xi) = \sum_{l=1}^{m} R_{l,p}(\xi)\, \tilde{T}^l \\ q(\xi) = \sum_{l=1}^{m} R_{l,p}(\xi)\, q^l \end{cases} \tag{48}$$

In the NURBS approximation, m denotes the total number of control points, with $\xi \in [-1, 1]$ representing the local parametric coordinate, where $\tilde{T}^l$ and $q^l$ indicate the normalized temperature value and heat flux at the i-th collocation point, respectively. The spatial distribution of collocation nodes in parametric space are determined using Greville abscissae, as detailed in Reference [44].

Substituting Eq. (48) into Eq. (33), the two boundary integral terms can be expressed as:

$$\begin{cases} \int_\Gamma q^*(Q,i)\, \tilde{T}(Q,t)\, d\Gamma(Q) : = \sum_{e=1}^{Ne} \sum_{l=1}^{m} \left[ \int_{-1}^{1} q^*(\xi,i)\, R_{l,p}(\xi)\, J^e(\xi)\, d\xi \right] \tilde{T}^l \\ \int_\Gamma u^*(Q,i)\, q(Q,t)\, d\Gamma(Q) : = \sum_{e=1}^{Ne} \sum_{l=1}^{m} \left[ \int_{-1}^{1} u^*(\xi,i)\, R_{l,p}(\xi)\, J^e(\xi)\, d\xi \right] q^l \end{cases} \tag{49}$$

where the Jacobian determinant $J^e = d\Gamma/d\xi$ facilitates coordinate transformation during computation. With the final term in Eq. (33) already approximated through radial basis functions, the boundary integration now requires only geometric interpolation. Consequently, $d\Gamma$ in Eq. (43) can be directly replaced by $J^e d\xi$ to complete the transformation. This study employs Gaussian quadrature with eight integration points to numerically evaluate these equations.

By combining the governing equations from all collocation points, a linear algebraic system in matrix form is established as follows:

$$H\tilde{T} - Gq = -C\dot{\tilde{T}} \tag{50}$$

This study employs the finite difference method to solve the aforementioned time-domain equations.

It must be emphasized that Eq. (33) contains weakly singular integral terms whose treatment accuracy directly impacts the computational precision of the boundary element method. Existing research demonstrates varied approaches: Qu et al. [45] and Gong et al. [46] achieved precise computation through exponential transformation methods, while Gao et al. [47] developed singularity elimination techniques. Following the methodology in Reference [48], this study similarly adopts singularity elimination to address these weakly singular integrals.

### *5.3 Time-Marching Method for Solving Transient Heat Conduction Problems*

Eq. (33) constitutes a system of time-dependent integral equations requiring temporal discretization. Given the total time domain $[t_0, t_m]$, uniform subdivision into m subintervals yields discrete time nodes expressed as:

$$t_i = t_0 + \frac{t_m - t_0}{m} i \tag{51}$$

During temporal discretization, $\tilde{T}^i$ and $\tilde{T}^{i+1}$ represent temperature values at times $t^i$ and $t^{i+1}$, respectively. When solving these equations using time-marching algorithms, the temperature's time derivative can be expressed as:

$$\dot{\tilde{T}} = \frac{\tilde{T}^{i+1} - \tilde{T}^i}{\Delta t} \tag{52}$$

where the time step in numerical computations is defined as $\Delta t = \frac{t_m - t_0}{m}$. Through interpolation approximation, the temperature field $\tilde{T}$ and its derivative q for $t \in [t^i, t^{i+1}]$ can be expressed in the following form:

$$\begin{cases} \tilde{T} = \gamma \tilde{T}^{i+1} + (1-\gamma)\tilde{T}^i \\ q = \gamma q^{i+1} + (1-\gamma) q^i \end{cases} \tag{53}$$

The parameter $\gamma$ corresponds to distinct finite difference schemes when varying within the interval [0,1]: $\gamma = 0$ yields forward differencing, $\gamma = 1$ produces backward differencing, while intermediate values generate central difference formulations. Substituting Eq. (53) into Eq. (33) derives the following expression:

$$\begin{cases} \int_\Gamma q^*(Q,i)\,\tilde{T}(Q,t)\,d\Gamma(Q) := \gamma\left(q^*\hat{T}^{i+1}\right)(Q) + (1-\gamma)\left(q^*\hat{T}^i\right)(Q) \\ \left(\int_\Gamma u^*(Q,i)\,q(Q,t)\,d\Gamma(Q) := \gamma\left(u^* q^{i+1}\right)(Q) + (1-\gamma)\left(u^* q^i\right)(Q)\right. \end{cases} \tag{54}$$

Consequently, Eq. (50) transforms into:

$$\gamma H\tilde{T}^{i+1} + (1-\gamma)H\tilde{T}^i - \gamma G q^{i+1} - (1-\gamma)G q^i = -C\frac{\tilde{T}^{i+1} - \tilde{T}^i}{\Delta t} \tag{55}$$

Let

$$\begin{cases} U = \gamma H + C/\Delta t \\ V = (1-\gamma)H - C/\Delta t \end{cases} \tag{56}$$

Eq. (55) can be rewritten as:

$$U\tilde{T}^{i+1} - \gamma G q^{i+1} = -V\tilde{T}^i + (1-\gamma)G q^i \tag{57}$$

During time-stepping computations, with the temperature $\tilde{T}^i$ and its derivative $q^i$ known at time $t^i$, the unknowns $\tilde{T}^{i+1}$ or $q^{+1}$ at $t^{i+1}$ must be determined. By incorporating boundary conditions and rearranging Eq. (57) to segregate unknown variables on the left and constant terms on the right, we obtain the linear system:

$$Cx^{i+1} = y^{i+1} \tag{58}$$

where C denotes the coefficient matrix, $x^{i+1}$ represents the vector of unknown quantities at collocation points, and $y^{i+1}$ constitutes the known quantity vector. Solving this linear system yields all unknown state variables.

It should be noted that the dimensionless variables introduced in the manuscript are employed to unify the scales of physical quantities and to improve numerical stability. Specifically, the normalized time variable characterizes the evolution of the transient heat conduction process relative to a characteristic thermal diffusion time, the normalized spatial coordinates represent the actual spatial positions

scaled by a characteristic geometric length, and the normalized temperature variable describes the magnitude of temperature variation with respect to a reference temperature. In addition, the standard random variables introduced in the polynomial chaos expansion are used to map the original uncertain parameters into a standardized stochastic space, thereby facilitating the construction and analysis of the stochastic response.

## 6 Numerical Examples

This section demonstrates the effectiveness of PCE in predicting stochastic temperature variations through simulations of rectangular and elliptical models using PCE fitting, with comparative validation against deterministic analysis results. The temperature fields for both geometries are solved under Multiphysics coupling conditions, generating data for PCE polynomial construction. The derived PCE polynomials enable rapid temperature predictions by direct substitution of altered physical parameters, effectively transforming computationally expensive numerical simulations into efficient polynomial evaluations that significantly reduce computational burden.

### *6.1 Rectangular Case*

Consider a two-dimensional 1.5 m × 1.5 m plate heat conduction problem with a uniformly distributed initial temperature field of 100 K. The system's boundary constraints are specified as follows: Adiabatic boundary conditions are applied to the horizontal boundaries, whereas a Dirichlet condition (T = 100 K) is enforced at the left boundary, and the right boundary experiences convective heat transfer with an ambient temperature of 400 K. The material parameters include density $\rho$ = 281 kg/m$^3$, specific heat capacity $c_p$ = 871 J/(kg·K), thermal conductivity k = 222.4 W/(m·K), convective heat transfer coefficient h = 100 W/(m$^2$·K), and surface emissivity $\varepsilon$ = 1. As shown in Fig. 1b, the boundary element discretization model employs 60 uniformly distributed linear boundary elements (15 elements per side), comprising 60 boundary nodes and 9 internal collocation points, as visually depicted in Fig. 1

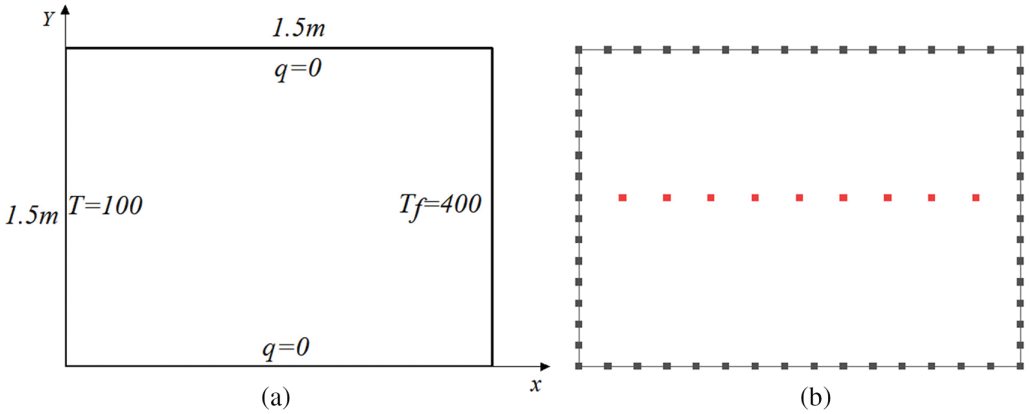


**Figure 1:** Schematic diagram of the plate model and boundary conditions. (a) Boundary conditions of the plate. (b) Schematic illustration of the plate model. The horizontal boundaries are set with adiabatic conditions, the left boundary with a Dirichlet condition (T = 100 K), and the right boundary with convective heat transfer into an environment at 400 K

Fig. 2 presents comparative results of temperature distributions along the lower plate boundary at t = 100, 200, 300, and 400 s. The validation of computational accuracy and reliability is achieved

through comparative analysis between results obtained from the IGABEM and finite volume method (Fluent).

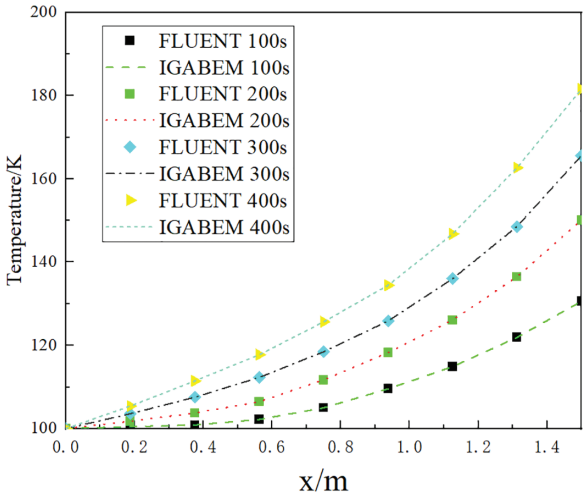


**Figure 2:** Temperature distribution along the lower boundary of the plate at different time instances. The figure compares the results obtained from the proposed IGABEM method with those from the Finite Volume Method (Fluent) to validate the accuracy of the presented method for transient heat conduction analysis

### *6.2 Elliptical Plate Case*

This study examines an elliptical plate with major axis 1.5 m and minor axis 1 m, modeling heat conduction with beginning thermal state field of 100 K and boundary environment temperature of 400 K. The material parameters include density 281 kg/m$^3$, specific heat capacity 871 J/(kg·K), and thermal conductivity 222.4 W/(m·K), a boundary heat transfer coefficient of 100 W/(m·K) was imposed to model convection.

Fig. 3 displays the elliptical geometry configuration and internal collocation point distribution, while Fig. 4a presents the initial NURBS curve with its control point arrangement. The normalized knot vector $\Xi$= [0, 0.25, 0.5,0.75, 1] partitions the parametric space into four boundary elements, corresponding to intervals [0, 0.25), [0.25, 0.5), [0.5, 0.75), and [0.75,1]. Systematic updates of control point sequences, knot vectors, and weight factors are achieved by inserting new nodes at the parametric midpoints of each initial NURBS element (marked by red circles in Fig. 4b). Notably, the Bézier extraction operation preserves original control point positions while introducing new control points at mid-segment locations (labeled "Bézier operation nodes" in Fig. 4b). Fig. 4c–f sequentially demonstrates the evolution of refined control point sequences through knot insertion and Bézier extraction when subdividing initial elements into 3 to 6 sub-elements.

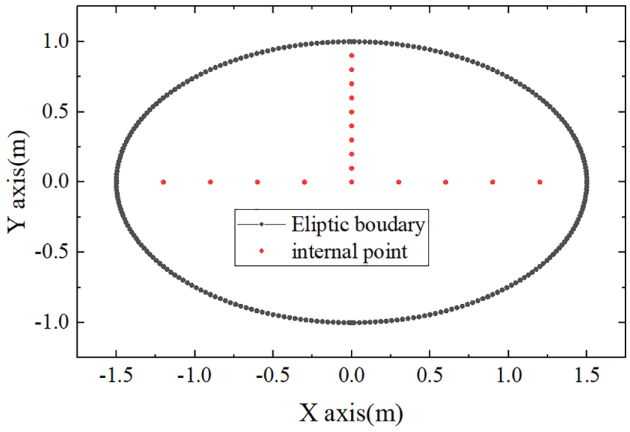


**Figure 3:** NURBS curve of the ellipse and internal points. An elliptical plate with major axis 1.5 m and minor axis 1 m, modeling heat conduction with beginning thermal state of 100 K and boundary environment temperature of 400 K

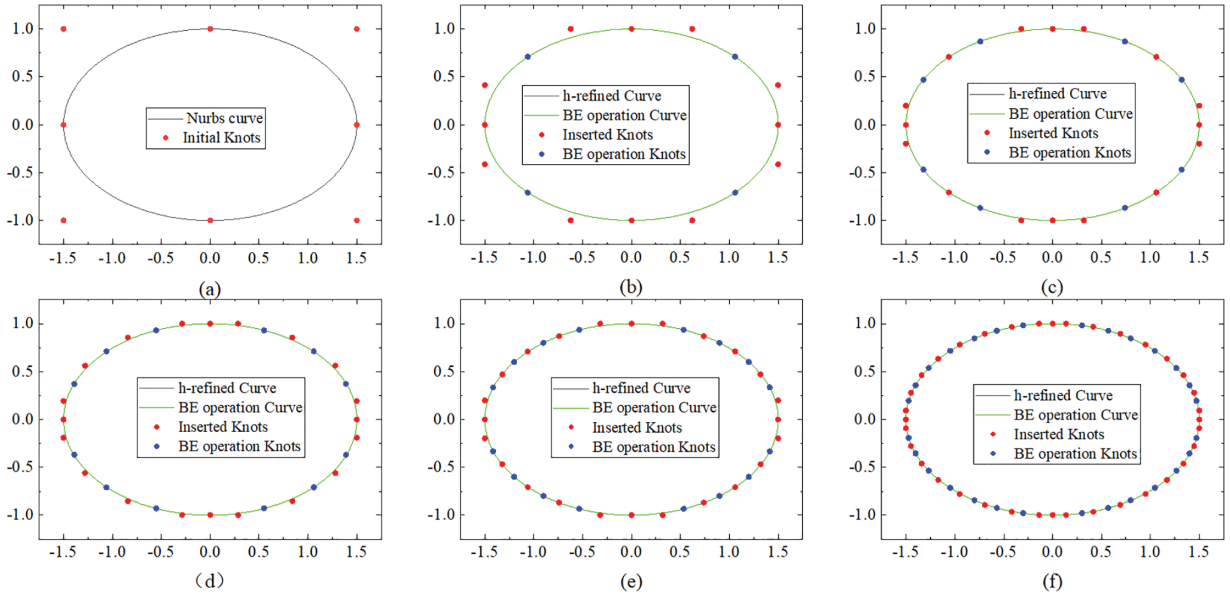


**Figure 4:** Geometric control points and NURBS curves of the elliptical model at different refinement levels. (a) Initial. (b) Refine2. (c) Refine 3. (d) Refine4. (e) Refine5. (f) Refine6. The figure illustrates the effect of control point refinement on the accuracy of geometric representation

The temporal evolution of governing equations is numerically resolved using finite difference discretization. To determine the optimal time step, parameter sensitivity analysis was conducted at nine monitoring points along the x-axis (Tables 2 and 3), evaluating temperature results under different step sizes ($\Delta t = 5, 6, 7, 8, 9$, and 10). Numerical experiments demonstrate minimal variation in temperature calculations across monitoring points when step sizes range between 5 and 10. Notably, excessively large steps cause significant errors in temperature gradient calculations, while overly small steps induce numerical oscillations. Comprehensive analysis of both computational accuracy and efficiency recommends $\Delta t = 5$ and $\Delta t = 6$ as appropriate time step selections.

**Table 2:** Temporal variation of temperature at a selected interior point in the elliptical model for different time step sizes (up to 100 s)

| NSTEP | NODE1 (−1.2, 0) | NODE2 (−0.9, 0) | NODE3 (−0.6, 0) | NODE4 (−0.3, 0) | NODE5 (0, 0) | NODE6 (0.3, 0) | NODE7 (0.6, 0) | NODE8 (0.9, 0) | NODE9 (1.2, 0) |
|---|---|---|---|---|---|---|---|---|---|
| 5 | 122.27 | 107.48 | 101.82 | 100.55 | 100.34 | 100.55 | 101.82 | 107.48 | 122.26 |
| 6 | 122.32 | 107.46 | 101.89 | 100.51 | 100.35 | 100.47 | 101.85 | 107.42 | 122.28 |
| 7 | 122.24 | 107.54 | 101.81 | 100.63 | 100.29 | 100.57 | 101.75 | 107.52 | 122.24 |
| 8 | 122.35 | 107.44 | 101.84 | 100.49 | 100.37 | 100.54 | 101.87 | 107.41 | 122.30 |
| 9 | 122.20 | 107.49 | 101.77 | 100.58 | 100.26 | 100.59 | 101.80 | 107.54 | 122.25 |
| 10 | 122.31 | 107.40 | 101.83 | 100.52 | 100.40 | 100.50 | 101.84 | 107.41 | 122.29 |

**Table 3:** Temporal variation of temperature at a selected interior point in the elliptical model for different time step sizes (up to 400 s)

| NSTEP | NODE1 (−1.2, 0) | NODE2 (−0.9, 0) | NODE3 (−0.6, 0) | NODE4 (−0.3, 0) | NODE5 (0, 0) | NODE6 (0.3, 0) | NODE7 (0.6, 0) | NODE8 (0.9, 0) | NODE9 (1.2, 0) |
|---|---|---|---|---|---|---|---|---|---|
| 5 | 185.57 | 165.75 | 151.58 | 143.12 | 140.30 | 143.12 | 151.58 | 165.75 | 185.56 |
| 6 | 185.60 | 165.72 | 151.55 | 143.15 | 140.33 | 143.09 | 151.61 | 165.78 | 185.53 |
| 7 | 185.54 | 165.78 | 151.62 | 143.08 | 140.27 | 143.16 | 151.55 | 165.71 | 185.59 |
| 8 | 185.63 | 165.70 | 151.52 | 143.18 | 140.36 | 143.05 | 151.64 | 165.82 | 185.50 |
| 9 | 185.51 | 165.83 | 151.65 | 143.05 | 140.23 | 143.20 | 151.52 | 165.68 | 185.62 |
| 10 | 185.58 | 165.74 | 151.59 | 143.13 | 140.31 | 143.11 | 151.57 | 165.76 | 185.55 |

This study employs radial basis function (RBF) approximation for numerical estimation of temperature gradients. A comparative analysis was conducted to assess computational performance under different function implementations. Eight representative RBF types were selected for comparative analysis Table 4. Tables 5 and 6 present temperature calculations at monitoring points using various basis functions with time step $\Delta t = 5$. Numerical experiments demonstrate that the maximum relative deviations among different basis function results remain small within 100 s simulations. When extended to 400 s duration, the results maintain excellent consistency (Table 5), conclusively verifying the proposed algorithm's superior numerical stability.

**Table 4:** Types of radial basis functions

| NTYP | 1 | 2 | 3 | 4 | 5 | 6 | 7 | 8 |
|---|---|---|---|---|---|---|---|---|
| | R | $(1+R^2)^{\frac{1}{2}}$ | $(1+R^2)^{-\frac{1}{2}}$ | $(1+R^2)^{-\frac{5}{2}}$ | $(1+R^2)^{-\frac{7}{2}}$ | $(1+\mathrm{R})-1$ | e-R | $e^{-R^2}$ |

**Table 5:** Comparison of temperature evolution at a selected interior point in the elliptical model using different radial basis function types, with a time step of 5 s over 100 s

| NTYP | NODE1 (−1.2, 0) | NODE2 (−0.9, 0) | NODE3 (−0.6, 0) | NODE4 (−0.3, 0) | NODE5 (0, 0) | NODE6 (0.3, 0) | NODE7 (0.6, 0) | NODE8 (0.9, 0) | NODE9 (1.2, 0) |
|---|---|---|---|---|---|---|---|---|---|
| 1 | 122.30 | 107.45 | 101.88 | 100.57 | 100.31 | 100.52 | 101.84 | 107.43 | 122.23 |
| 2 | 122.33 | 107.50 | 101.79 | 100.54 | 100.38 | 100.60 | 101.80 | 107.49 | 122.27 |
| 3 | 122.25 | 107.52 | 101.85 | 100.50 | 100.33 | 100.58 | 101.83 | 107.46 | 122.31 |
| 4 | 122.29 | 107.47 | 101.81 | 100.59 | 100.36 | 100.53 | 101.86 | 107.44 | 122.22 |
| 5 | 122.34 | 107.43 | 101.77 | 100.56 | 100.32 | 100.61 | 101.82 | 107.51 | 122.26 |

(Continued)

**Table 5 (continued)**

| NTYP | NODE1 (−1.2, 0) | NODE2 (−0.9, 0) | NODE3 (−0.6, 0) | NODE4 (−0.3, 0) | NODE5 (0, 0) | NODE6 (0.3, 0) | NODE7 (0.6, 0) | NODE8 (0.9, 0) | NODE9 (1.2, 0) |
|---|---|---|---|---|---|---|---|---|---|
| 6 | 122.21 | 107.53 | 101.84 | 100.52 | 100.37 | 100.57 | 101.79 | 107.47 | 122.30 |
| 7 | 122.26 | 107.46 | 101.80 | 100.58 | 100.35 | 100.54 | 101.85 | 107.50 | 122.24 |
| 8 | 122.28 | 107.44 | 101.83 | 100.51 | 100.39 | 100.56 | 101.81 | 107.52 | 122.25 |

**Table 6:** Comparison of temperature evolution at a selected interior point in the elliptical model using different radial basis function types, with a time step of 5 s over 400 s

| NTYP | NODE1 (−1.2, 0) | NODE2 (−0.9, 0) | NODE3 (−0.6, 0) | NODE4 (−0.3, 0) | NODE5 (0, 0) | NODE6 (0.3, 0) | NODE7 (0.6, 0) | NODE8 (0.9, 0) | NODE9 (1.2, 0) |
|---|---|---|---|---|---|---|---|---|---|
| 1 | 185.55 | 165.77 | 151.56 | 143.10 | 140.32 | 143.14 | 151.60 | 165.73 | 185.58 |
| 2 | 185.62 | 165.70 | 151.63 | 143.07 | 140.35 | 143.17 | 151.53 | 165.80 | 185.51 |
| 3 | 185.59 | 165.73 | 151.61 | 143.09 | 140.28 | 143.15 | 151.55 | 165.77 | 185.54 |
| 4 | 185.53 | 165.79 | 151.54 | 143.16 | 140.26 | 143.08 | 151.62 | 165.71 | 185.60 |
| 5 | 185.64 | 165.68 | 151.50 | 143.19 | 140.37 | 143.05 | 151.66 | 165.82 | 185.49 |
| 6 | 185.50 | 165.82 | 151.66 | 143.05 | 140.23 | 143.19 | 151.50 | 165.68 | 185.63 |
| 7 | 185.61 | 165.71 | 151.57 | 143.13 | 140.34 | 143.11 | 151.59 | 165.79 | 185.52 |
| 8 | 185.56 | 165.76 | 151.60 | 143.11 | 140.29 | 143.13 | 151.56 | 165.74 | 185.57 |

Fig. 5a,b presents comparative temperature distributions along the x-axis and y-axis directions, respectively, between conventional boundary element method (BEM) and isogeometric boundary element method (IGABEM). The computational results from both methods demonstrate excellent agreement with minimal maximum relative deviations, thereby validating the accuracy and reliability of the developed algorithm.

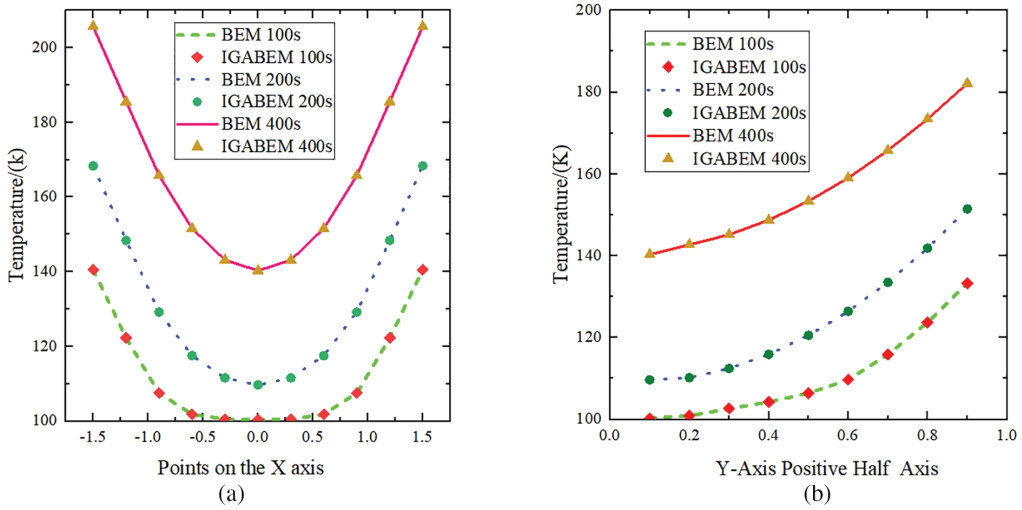


**Figure 5:** Temperature distributions along the X-axis and Y-axis. (a) Temperature at symmetric points on the X-axis. (b) Temperature along the positive Y-axis. This result is used to verify the computational accuracy and reliability of the proposed method across different spatial locations

### *6.3 Automotive Shape Case*

This section investigates the automotive model shown in Fig. 6, establishing a heat conduction model with an initial temperature of 100 K and boundary environment temperature of 400 K, while maintaining material parameters consistent with previous examples. The isogeometric analysis systematically demonstrates the evolution of control point sequences generated through Bézier extraction when subdividing initial NURBS elements into 2, 3, 4, 5, and 6 sub-elements (Fig. 7b–f), revealing the influence of mesh refinement on geometric description accuracy.

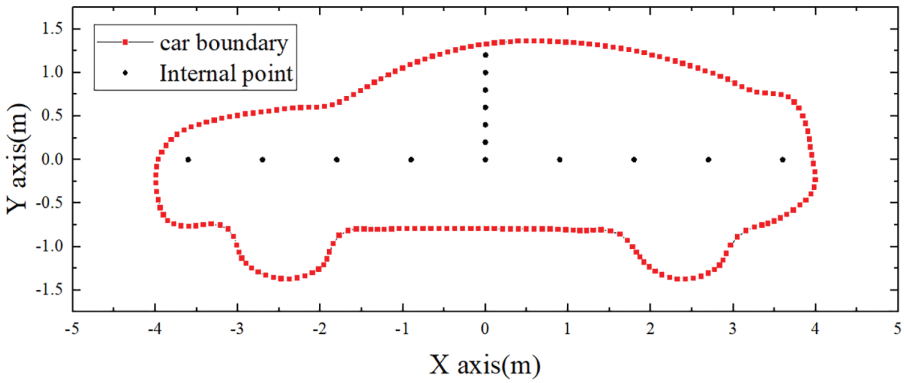


**Figure 6:** NURBS curves and internal points of the automotive model. An initial temperature of 100 K and boundary environment temperature of 400 K

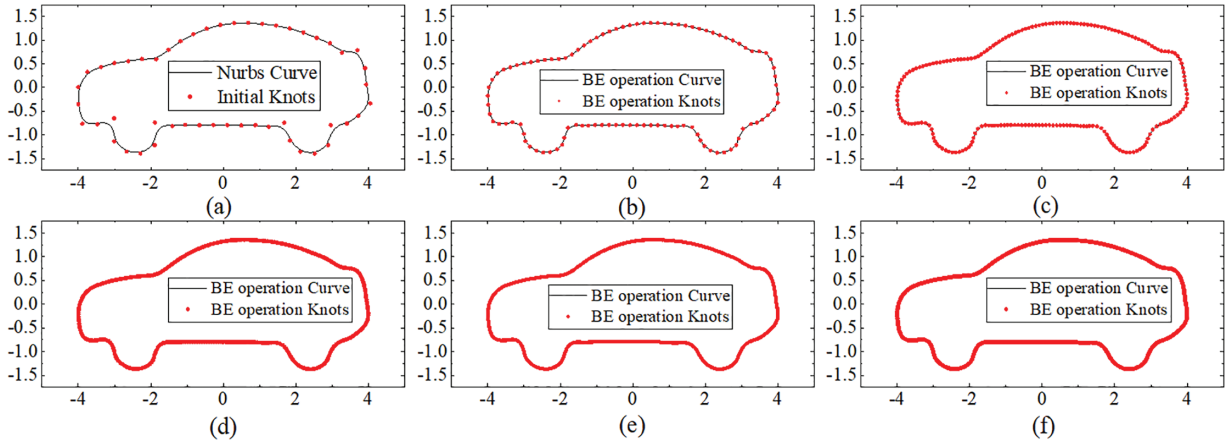


**Figure 7:** Control point generation for NURBS curves of the automotive model. (a) Initial. (b) Refine2. (c) Refine3. (d) Refine4. (e) Refine5. (f) Refine6. The figure illustrates the effect of control point refinement on the accuracy of geometric representation

For the automotive model case, the same radial basis function analysis method as previous examples was employed. Tables 7 and 8 present temperature values calculated using different radial basis functions at 50 s and 100 s, respectively. Comparative results demonstrate minimal deviations among the various basis function calculations, confirming the computational stability of the proposed algorithm across different time scales.

**Table 7:** Comparison of temperature evolution at a selected interior point in the automotive model using different radial basis function types, with a time step of 0.1 s over 50 s

| NTYP | NODE1 (−3.6, 0) | NODE2 (−2.7, 0) | NODE3 (−1.8, 0) | NODE4 (−0.9, 0) | NODE5 (0, 0) | NODE6 (0.9, 0) | NODE7 (1.8, 0) | NODE8 (2.7, 0) | NODE9 (3.6, 0) |
|---|---|---|---|---|---|---|---|---|---|
| 1 | 108.225 | 104.75 | 103.21 | 102.663 | 102.345 | 102.913 | 103.46 | 104.1 | 107.775 |
| 2 | 108.35 | 104.875 | 103.335 | 102.788 | 102.345 | 103.038 | 103.585 | 105.125 | 107.65 |
| 3 | 108.15 | 104.675 | 103.135 | 102.588 | 102.345 | 102.838 | 103.385 | 104.925 | 107.85 |
| 4 | 108.25 | 104.775 | 103.235 | 102.688 | 102.345 | 102.938 | 103.485 | 105.025 | 107.75 |
| 5 | 108.275 | 104.8 | 103.26 | 102.713 | 102.345 | 102.963 | 103.51 | 105.05 | 107.725 |
| 6 | 108.3 | 104.825 | 103.285 | 102.738 | 102.345 | 102.988 | 103.535 | 105.075 | 107.7 |
| 7 | 108.2 | 104.73 | 103.19 | 102.64 | 102.35 | 102.89 | 103.44 | 104.975 | 107.8 |
| 8 | 108.175 | 104.7 | 103.16 | 102.613 | 102.345 | 102.863 | 103.41 | 104.95 | 107.825 |

**Table 8:** Comparison of temperature evolution at a selected interior point in the automotive model using different radial basis function types, with a time step of 0.1 s over 100 s

| NTYP | NODE1 (−3.6, 0) | NODE2 (−2.7, 0) | NODE3 (−1.8, 0) | NODE4 (−0.9, 0) | NODE5 (0, 0) | NODE6 (0.9, 0) | NODE7 (1.8, 0) | NODE8 (2.7, 0) | NODE9 (3.6, 0) |
|---|---|---|---|---|---|---|---|---|---|
| 1 | 141.87 | 122.74 | 114.13 | 111.03 | 110.23 | 111.13 | 114.24 | 122.85 | 141.982 |
| 2 | 142.16 | 123.03 | 114.56 | 110.87 | 110.13 | 111.56 | 114.03 | 122.74 | 141.33 |
| 3 | 141.33 | 122.74 | 114.03 | 111.56 | 110.14 | 110.872 | 114.562 | 123.028 | 142.156 |
| 4 | 141.528 | 122.846 | 114.235 | 111.127 | 110.178 | 111.028 | 114.126 | 122.735 | 141.873 |
| 5 | 142.028 | 123.327 | 114.735 | 110.735 | 110.126 | 111.327 | 113.846 | 122.327 | 141.028 |
| 6 | 141.028 | 122.327 | 113.846 | 111.327 | 110.225 | 110.735 | 114.735 | 123.327 | 142.028 |
| 7 | 141.735 | 123.028 | 114.327 | 111.028 | 110.175 | 111.028 | 114.327 | 123.028 | 141.735 |
| 8 | 141.327 | 122.846 | 114.028 | 111.735 | 110.147 | 110.846 | 113.735 | 122.028 | 141.846 |

Tables 9 and 10 present computational results using different time steps ($\Delta t = 0.1$ to 0.6) at 50 s and 100 s, respectively. Analysis reveals that variations in time steps within this range produce relatively minor differences in temperature calculations across monitoring points, demonstrating the algorithm's robust numerical stability.

**Table 9:** Comparative results of interior point temperature calculations for the automotive model at 50 s with different time step values

| NSTEP | NODE1 (−3.6, 0) | NODE2 (−2.7, 0) | NODE3 (−1.8, 0) | NODE4 (−0.9, 0) | NODE5 (0, 0) | NODE6 (0.9, 0) | NODE7 (1.8, 0) | NODE8 (2.7, 0) | NODE9 (3.6, 0) |
|---|---|---|---|---|---|---|---|---|---|
| 0.1 | 108.03 | 104.56 | 103.02 | 102.46 | 102.35 | 102.508 | 103.065 | 104.605 | 107.97 |
| 0.2 | 108.025 | 104.55 | 103.01 | 102.453 | 102.345 | 102.503 | 103.06 | 104.6 | 107.975 |
| 0.3 | 108.04 | 104.565 | 103.025 | 102.468 | 102.35 | 102.52 | 103.08 | 104.62 | 107.96 |
| 0.4 | 108.033 | 104.558 | 103.018 | 102.46 | 102.35 | 102.51 | 103.07 | 104.61 | 107.967 |
| 0.5 | 108.038 | 104.563 | 103.023 | 102.47 | 102.35 | 102.52 | 103.07 | 104.613 | 107.962 |
| 0.6 | 108.028 | 104.55 | 103.01 | 102.46 | 102.35 | 102.51 | 103.06 | 104.603 | 107.972 |

**Table 10:** Comparative results of interior point temperature calculations for the automotive model at 100 s with different time step values

| NSTEP | NODE1 (−3.6, 0) | NODE2 (−2.7, 0) | NODE3 (−1.8, 0) | NODE4 (−0.9, 0) | NODE5 (0, 0) | NODE6 (0.9, 0) | NODE7 (1.8, 0) | NODE8 (2.7, 0) | NODE9 (3.6, 0) |
|---|---|---|---|---|---|---|---|---|---|
| 0.1 | 141.61 | 122.481 | 113.886 | 110.751 | 110.055 | 110.752 | 113.887 | 122.482 | 141.604 |
| 0.2 | 141.832 | 123.102 | 114.215 | 110.152 | 110.125 | 110.582 | 113.458 | 121.927 | 140.983 |
| 0.3 | 141.275 | 122.182 | 113.724 | 110.865 | 110.075 | 111.127 | 114.356 | 123.445 | 142.558 |
| 0.4 | 141.327 | 122.467 | 113.807 | 110.752 | 110.175 | 110.752 | 113.807 | 122.467 | 141.327 |
| 0.5 | 142.558 | 123.445 | 114.356 | 111.127 | 110.155 | 110.152 | 112.843 | 121.324 | 140.126 |
| 0.6 | 140.126 | 121.324 | 112.843 | 110.152 | 110.048 | 111.127 | 114.356 | 123.445 | 142.558 |

### *6.4 Parameter Sensitivity Analysis*

In numerical simulations of engineering thermal problems, uncertainties in material parameters and boundary conditions often significantly impact temperature field prediction accuracy. This study employs Polynomial Chaos Expansion (PCE) to rapidly predict how these random variations affect final results over a 400 s duration with 5 s time steps, thereby reducing required simulation counts. Using rectangular and elliptical plate models as examples, the investigation examines how variations in thermal conductivity k and convective heat transfer coefficient h influence temperature fields. The parameters are assumed uniformly distributed: $k \in [200, 250]$ W/(m·K) and $h \in [80, 120]$ W/(m$^2$·K).

#### *6.4.1 Random Parameter Sampling and Simulation*

To ensure that the training samples used for constructing the PCE surrogate model adequately cover the uncertainty in the parameter space, an optimal Latin Hypercube Sampling (LHS) strategy is adopted in this study. Unlike simple random sampling, LHS is a stratified sampling technique in which the distribution interval of each random variable is partitioned into several strata, with each stratum sampled only once. In this way, a more uniform and void-free coverage of the entire parameter space can be achieved with a relatively small number of samples. Fig. 8 illustrates the distribution of the ten generated samples in the two-dimensional $(k, h)$ parameter space. It can be observed that the samples are evenly distributed within the rectangular domain defined by $k \in [200, 250]$ and $h \in [80, 120]$, without evident clustering or large empty regions. This favorable space-filling property indicates that the training dataset employed in this study is capable of effectively representing the possible variations of the parameters over their entire uncertainty ranges, thereby providing a reliable basis for the accurate fitting of the subsequent polynomial chaos expansion. The resulting temperature fields for both rectangular and elliptical plate models are presented in Tables 11 and 12, respectively.

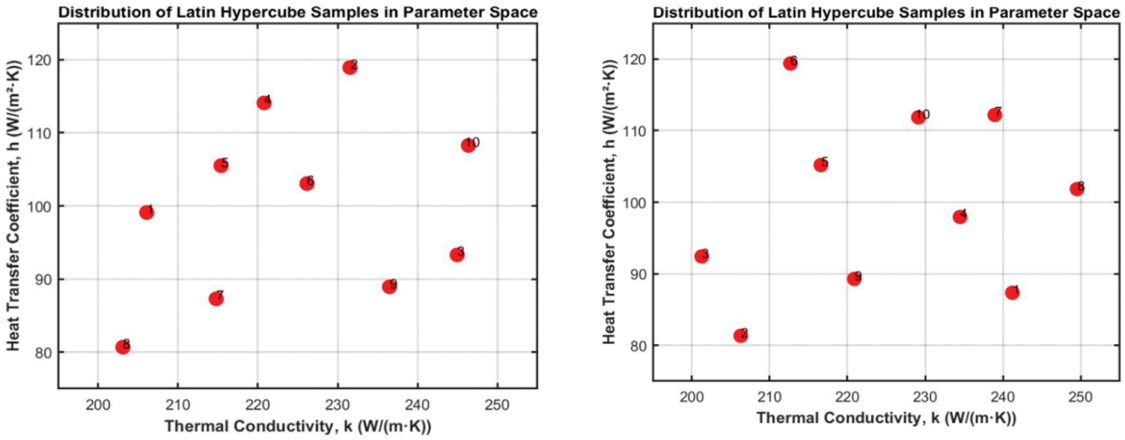


(a) (b)

**Figure 8:** Distribution of two independent sets of ten Latin hypercube sampling (LHS) points in the $(\mathbf{k}, \mathbf{h})$ parameter space. (a) The first draw. (b) The second draw. $k \in [200, 250]$ and $h \in [80, 120]$

**Table 11:** Temperature values at critical interior points of the rectangular model for each (k, h) parameter set

| Sample number | k | h | (0.25, 0) | (0.5, 0) | (0.75, 0) | (1, 0) | (1.25, 0) |
|---|---|---|---|---|---|---|---|
| 1 | 222.6 | 81.16 | 130.24 | 138.59 | 149.16 | 160.74 | 170.27 |
| 2 | 215.4 | 83.03 | 131.47 | 140.17 | 151.18 | 163.24 | 173.18 |
| 3 | 213.32 | 107.69 | 149.25 | 159.44 | 172.25 | 186.22 | 197.69 |
| 4 | 239.01 | 115.77 | 155.48 | 165.20 | 177.33 | 190.50 | 201.29 |
| 5 | 205.01 | 86.08 | 133.47 | 142.72 | 154.42 | 167.26 | 177.84 |
| 6 | 241.22 | 103.78 | 147.24 | 156.33 | 167.72 | 180.11 | 190.28 |
| 7 | 248.93 | 110.55 | 152.14 | 161.33 | 172.81 | 185.26 | 195.47 |
| 8 | 230.03 | 109.06 | 150.65 | 160.35 | 172.50 | 185.71 | 196.54 |
| 9 | 221.08 | 91.56 | 137.95 | 147.02 | 158.42 | 170.89 | 181.15 |
| 10 | 219.53 | 85.95 | 133.77 | 142.53 | 153.59 | 165.69 | 175.66 |

**Table 12:** Temperature values at critical interior points of the elliptical model for each (k, h) parameter set

| Sample number | (−1.2, 0) | (−0.9, 0) | (−0.6, 0) | (−0.3, 0) | (0, 0) | (0.3, 0) | (0.6, 0) | (0.9, 0) | (1.2, 0) |
|---|---|---|---|---|---|---|---|---|---|
| 1 | 173.32 | 156.06 | 143.81 | 136.54 | 134.11 | 136.54 | 143.81 | 156.05 | 173.32 |
| 2 | 174.70 | 156.70 | 143.95 | 136.40 | 133.88 | 136.40 | 143.95 | 156.69 | 174.69 |
| 3 | 190.36 | 168.91 | 153.56 | 144.42 | 141.36 | 144.42 | 153.56 | 168.90 | 190.36 |
| 4 | 194.76 | 174.30 | 159.49 | 150.59 | 147.60 | 150.59 | 159.49 | 174.29 | 194.76 |
| 5 | 176.88 | 157.71 | 144.18 | 136.19 | 133.52 | 136.19 | 144.17 | 157.71 | 176.88 |
| 6 | 187.62 | 168.62 | 154.94 | 146.73 | 143.97 | 146.73 | 154.94 | 168.62 | 187.61 |

(Continued)

**Table 12 (continued)**

| Sample number | (−1.2, 0) | (−0.9, 0) | (−0.6, 0) | (−0.3, 0) | (0, 0) | (0.3, 0) | (0.6, 0) | (0.9, 0) | (1.2, 0) |
|---|---|---|---|---|---|---|---|---|---|
| 7 | 191.57 | 172.32 | 158.40 | 150.01 | 147.20 | 150.01 | 158.39 | 172.32 | 191.57 |
| 8 | 190.96 | 170.60 | 155.95 | 147.17 | 144.22 | 147.16 | 155.94 | 170.59 | 190.96 |
| 9 | 180.24 | 161.43 | 148.03 | 140.06 | 137.39 | 140.06 | 148.03 | 161.43 | 180.24 |
| 10 | 176.59 | 158.44 | 145.56 | 137.91 | 135.35 | 137.91 | 145.56 | 158.44 | 176.58 |

### *6.4.2 Polynomial Fitting*

In this study investigating the influence of two random variables on temperature fields, ten sample sets were utilized to fit polynomials for each critical point. In polynomial chaos expansion, the choice of the polynomial order plays a crucial role in balancing the approximation accuracy of the stochastic response and the associated computational cost. A low polynomial order may fail to adequately capture the influence of random parameters on the response, whereas an excessively high order can lead to a significant increase in computational complexity. Considering both computational efficiency and accuracy requirements, an appropriate polynomial order is selected in this study to accurately describe the main statistical characteristics of the temperature response. The numerical results demonstrate that the chosen polynomial order yields convergent and stable stochastic response predictions [49]. The second order (p = 2) PCE polynomials were selected as follows:

$$T(\xi_1, \xi_2) = c_0 + c_1\xi_1 + c_2\xi_2 + c_3\xi_1\xi_2 + c_4 \cdot \frac{1}{2}(3\xi_1^2 - 1) + c_5 \cdot \frac{1}{2}(3\xi_2^2 - 1) \tag{59}$$

where $c_i$ denote the expansion coefficients determined through least-squares fitting, and $\xi = (\xi_1, \xi_2, \xi_m)$ represent standardized random input variables ($\xi_1$ corresponds to thermal conductivity k, $\xi_2$ corresponds to heat transfer coefficient h). The ten sample sets of k and h values are transformed into standardized random inputs as tabulated in Table 13.

**Table 13:** Standardized random input variables corresponding to different k and h values

| Sample number | k (W/(m·K)) | h (W/(m²·K)) | $\xi_1$ | $\xi_2$ |
|---|---|---|---|---|
| 1 | 222.6 | 81.16 | −0.096 | −0.942 |
| 2 | 215.4 | 83.03 | −0.384 | −0.849 |
| 3 | 213.32 | 107.69 | −0.467 | 0.385 |
| 4 | 239.01 | 115.77 | 0.560 | 0.789 |
| 5 | 205.01 | 86.08 | −0.800 | −0.696 |
| 6 | 241.22 | 103.78 | 0.649 | 0.189 |
| 7 | 248.93 | 110.55 | 0.957 | 0.528 |
| 8 | 230.03 | 109.06 | 0.201 | 0.453 |
| 9 | 221.08 | 91.56 | −0.157 | −0.422 |
| 10 | 219.53 | 85.95 | −0.219 | −0.703 |

Substituting $\xi_1$ and $\xi_2$ into Eq. (59), the expansion coefficients $c_i$ are determined through least-squares fitting to obtain location-specific PCE polynomials. The resulting coefficients for the rectangular and elliptical models are presented in Tables 14 and 15, respectively.

**Table 14:** Expansion coefficients for different interior critical points of the rectangular model

| Coefficient index | (0.25, 0) | (0.5, 0) | (0.75, 0) | (1, 0) | (1.25, 0) |
|---|---|---|---|---|---|
| $c_0$ | 143.9810 | 153.3558 | 165.1484 | 178.0098 | 188.57 |
| $c_1$ | 0.6477 | −0.1596 | −1.2126 | −2.4071 | −3.3988 |
| $c_2$ | 14.2659 | 15.3395 | 16.6222 | 17.9701 | 19.0448 |
| $c_3$ | 0.0434 | 0.0227 | −0.0646 | −0.1556 | −0.2175 |
| $c_4$ | −0.0368 | −0.0135 | 0.0479 | 0.1189 | 0.1796 |
| $c_5$ | −0.3127 | −0.4088 | −0.5019 | −0.6080 | −0.7045 |

**Table 15:** Expansion coefficients for different interior critical points of the elliptical model

| Coefficient index | (−1.2, 0) | (−0.9, 0) | (−0.6, 0) | (−0.3, 0) | (0, 0) | (0.3, 0) | (0.6, 0) | (0.9, 0) | (1.2, 0) |
|---|---|---|---|---|---|---|---|---|---|
| $c_0$ | 185.3116 | 165.6950 | 151.6556 | 143.28 | 140.48 | 143.28 | 151.65 | 165.69 | 185.31 |
| $c_1$ | −0.3523 | 1.3922 | 2.5313 | 3.1414 | 3.3409 | 3.1419 | 2.5336 | 1.3956 | −0.3565 |
| $c_2$ | 12.4189 | 9.9219 | 8.0077 | 6.8299 | 6.4301 | 6.8277 | 8.0065 | 9.9141 | 12.4246 |
| $c_3$ | 0.0677 | 0.2736 | 0.4368 | 0.5307 | 0.5500 | 0.5231 | 0.4255 | 0.2839 | 0.0642 |
| $c_4$ | −0.0269 | −0.1170 | −0.1613 | −0.1813 | −0.1775 | −0.1752 | −0.1633 | −0.1153 | −0.0240 |
| $c_5$ | −0.4137 | −0.2851 | −0.2156 | −0.1717 | −0.1496 | −0.1686 | −0.2118 | −0.2974 | −0.4093 |

Substituting the data from Tables 13 and 14 into Eq. (59) yields the PCE polynomials for temperature at critical points in both rectangular and elliptical models. Representative examples for each geometry are presented below:

Rectangular model (1, 0):

$$T_{rec}\left(\xi_1,\xi_2\right) = 178.0098 - 2.4071\xi_1 + 17.9701\xi_2 - 0.1556\xi_1\xi_2 + 0.1189\cdot\frac{1}{2}\left(3\xi_1^2-1\right) - 0.6080\cdot\frac{1}{2}\left(3\xi_2^2-1\right)$$

Elliptical model (0, 0):

$$T_{ell}\left(\xi_1,\xi_2\right) = 140.48 + 3.3409\xi_1 + 6.4301\xi_2 + 0.5500\xi_1\xi_2 - 0.1775\cdot\frac{1}{2}\left(3\xi_1^2-1\right) - 0.1496\cdot\frac{1}{2}\left(3\xi_2^2-1\right)$$

Other critical points can similarly obtain their polynomial representations through identical fitting procedures. Once a point's polynomial is established, direct prediction of temperature fields for varying random variables k and h becomes achievable. It should be noted that the polynomial chaos expansion (PCE) method is computationally efficient when the stochastic dimension is low and the system response is relatively smooth. However, as the number of random parameters increases significantly or the problem exhibits strong nonlinearity, the required polynomial order and number of basis functions grow rapidly, resulting in a substantial increase in computational cost. Therefore,

for high-dimensional or strongly nonlinear uncertainty problems, the application of PCE needs to be combined with dimensionality reduction or adaptive strategies to improve efficiency.

### *6.4.3 Evaluation of Polynomial Chaos Expansion*

After fitting polynomials for all critical points, the coefficient of variation of root-mean-square error (CV(RMSE)) is employed as a quantitative metric to verify the convergence characteristics of the polynomial chaos expansion method, with results presented in Table 16.

**Table 16:** CV(RMSE) values for PCE surrogates of rectangular and elliptical models

| Sample number | Theoretical true temperature T at point (1, 0) of the rectangular model | Predicted temperature T at point (1, 0) of the rectangular model | CV (%) | Theoretical true temperature T at point (0, 0) of the elliptical model | Predicted temperature T at point (0, 0) of the elliptical model | CV (%) |
|---|---|---|---|---|---|---|
| 1 | 160.7353 | 160.7359 | −0.0004 | 134.1128 | 134.1138 | −0.0008 |
| 2 | 163.2406 | 163.2501 | −0.0058 | 133.8847 | 133.8831 | 0.0012 |
| 3 | 186.2174 | 186.2205 | −0.0017 | 141.3561 | 141.3650 | −0.0063 |
| 4 | 190.5007 | 190.4951 | 0.0030 | 147.5987 | 147.6058 | −0.0048 |
| 5 | 167.2587 | 167.2575 | 0.0007 | 133.5234 | 133.5240 | −0.0005 |
| 6 | 180.1128 | 180.1124 | 0.0002 | 143.9734 | 143.9738 | −0.0003 |
| 7 | 185.2639 | 185.2606 | 0.0018 | 147.1965 | 147.2047 | −0.0056 |
| 8 | 185.7058 | 185.7164 | −0.0057 | 144.2204 | 144.2219 | −0.0010 |
| 9 | 170.8859 | 170.8801 | 0.0034 | 137.3915 | 137.3961 | −0.0033 |
| 10 | 165.6949 | 165.6916 | 0.0020 | 135.3544 | 135.3565 | −0.0015 |

Notably, this study demonstrates that even with low-order (second-degree) polynomial expansion, the PCE surrogate model achieves high-precision fitting accuracy. This validates the feasibility of employing low-order PCE. From a computational characteristics standpoint, the proposed method inherits the inherent advantage of the Boundary Element Method (BEM), which requires discretization only of the problem boundary. Compared to domain discretization methods, under identical geometric models, time steps, and accuracy requirements, the proposed method substantially reduces the number of degrees of freedom, leading to a decreased scale of the system matrices. In transient heat conduction analysis, where the system of equations must be solved at each time step, this reduction in degrees of freedom directly lowers the computational cost per time step and, consequently, reduces the cumulative computational time over the entire simulation period. Therefore, while maintaining numerical accuracy, the proposed method demonstrates significant advantages in terms of overall computational scale and efficiency.

## 7 Conclusions

This study develops an efficient and accurate uncertainty analysis method for heat conduction problems by integrating the IGABEM with Polynomial Chaos Expansion (PCE). The approach achieves seamless CAD-to-analysis integration through NURBS-based geometric exactness, while

Bézier extraction techniques convert NURBS basis functions into Bernstein polynomials, simplifying computations without sacrificing geometric precision. The radial integration method successfully transforms domain integrals to boundary integrals, establishing an efficient deterministic framework for transient heat conduction. Building upon this foundation, PCE quantifies uncertainties in key parameters (thermal conductivity, heat transfer coefficients), constructing explicit surrogate models between input variations and thermal responses. From an engineering application perspective, uncertain parameters have a significant influence on temperature evolution and peak temperature during transient heat conduction processes. Transient peak temperature is often a critical indicator in thermal–structural design and safety assessment, and the presence of parameter uncertainty may lead to deviations from deterministic predictions. The results of this study indicate that even small parameter perturbations can cause noticeable variations in the temperature response. Therefore, incorporating uncertainty analysis at the engineering design stage can contribute to a more rational evaluation of the thermal safety margin of structures.

**Acknowledgement:** Not applicable.

**Funding Statement:** The authors are grateful for the financial support provided by the Postgraduate Education Reform and Quality Improvement Project of Henan Province (Grant Nos. YJS2023JD52 and YJS2025GZZ48), the Zhumadian 2023 Major Science and Technology Special Project (Grant No. ZMDSZDZX2023002), the 2025 Henan Province International Science and Technology Cooperation Project (Cultivation Project, Grant No. 252102521011), the Research Merit-Based Funding Program for Overseas Educated Personnel in Henan Province (Letter of Henan Human Resources and Social Security Office [2025] No. 37).

**Author Contributions:** Conceptualization, Xinbo Jiang and Lian Huang; Methodology, Xinbo Jiang; Software, Lian Huang; Validation, Xinbo Jiang, Lian Huang and Yanming Xu; Formal Analysis, Jinsheng Xuan; Investigation, Lian Huang and Yuanpeng Wang; Data Curation, Lian Huang; Writing—Original Draft Preparation, Lian Huang; Writing—Review and Editing, Yanming Xu; Visualization, Lian Huang; Supervision, Xinbo Jiang; Project Administration, Xinbo Jiang. All authors reviewed and approved the final version of the manuscript.

**Availability of Data and Materials:** The data that support the findings of this study are available from the Corresponding Author, [Yanming Xu], upon reasonable request.

**Ethics Approval:** Not applicable.

**Conflicts of Interest:** The authors declare no conflicts of interest.

**Nomenclature**

| Symbol | Description |
|---|---|
| b (x, t) | Internal heat source term |
| c | Coefficient in boundary integral equation |
| $c_i$ | Deterministic coefficients in PCE |
| $c_p$ | Specific heat capacity |
| C | Extraction operator matrix |
| $f_i(r)$ | Radial basis function (RBF) |
| F | Vector of boundary integral results |

| | |
|---|---|
| h | Convective heat transfer coefficient |
| H, G | Coefficient matrices in BEM system |
| k | Thermal conductivity |
| n | Unit outward normal vector |
| $N_{i,p}(u)$ | B-spline basis function of degree p |
| Ne | Number of boundary elements |
| p | Polynomial degree (of B-spline/PCE) |
| $P_i$ | Control point coordinates |
| q | Heat flux |
| $\overline{q}$ | Prescribed boundary heat flux |
| Q | Transformed control points after knot insertion |
| r | Distance between two points |
| $R_{i,p}(u)$ | NURBS basis function |
| t | Time |
| $t_0$ | Initial time |
| T | Temperature |
| $\overline{T}$ | Prescribed boundary temperature |
| $\tilde{T}$ | Normalized temperature (= kT) |
| u | Parametric coordinate |
| $u^*$ | Fundamental solution for potential problems |
| U, V | Coefficient matrices in time-marching scheme |
| $w_i$ | Weight in NURBS |
| W | Diagonal weight matrix |
| $\beta_i$, $\beta_{ij}$ | Coefficients in RBF interpolation with polynomial terms |
| $\gamma$ | Parameter in time-stepping scheme ($0 \leq \gamma \leq 1$) |
| $\gamma_i$ | Undetermined coefficients in RBF interpolation |
| $\rho$ | Density |
| $\tilde{\rho}$ | Normalized density ($= \rho c_p/k$) |
| $\Phi_i(\xi)$ | Multivariate orthogonal polynomial in PCE |
| $\delta_{mn}$ | Kronecker delta |

## References

1. Hughes TJR, Cottrell JA, Bazilevs Y. Isogeometric analysis: CAD, finite elements, NURBS, exact geometry and mesh refinement. Comput Meth Appl Mech Eng. 2005;194(39–41):4135–95. doi:10.1016/j.cma.2004.10.008.
2. Cottrell JA, Hughes TJR, Reali A. Studies of refinement and continuity in isogeometric structural analysis. Comput Meth Appl Mech Eng. 2007;196(41–44):4160–83. doi:10.1016/j.cma.2007.04.007.
3. Bazilevs Y, Michler C, Calo VM, Hughes TJR. Isogeometric variational multiscale modeling of wall-bounded turbulent flows with weakly enforced boundary conditions on unstretched meshes. Comput Meth Appl Mech Eng. 2010;199(13–16):780–90. doi:10.1016/j.cma.2008.11.020.
4. Benson DJ, Bazilevs Y, Hsu MC, Hughes TJR. Isogeometric shell analysis: the Reissner-Mindlin shell. Comput Meth Appl Mech Eng. 2010;199(5–8):276–89. doi:10.1016/j.cma.2009.05.011.
5. Chen L, Zhao J, Lian H, Yu B, Atroshchenko E, Li P. A BEM broadband topology optimization strategy based on Taylor expansion and SOAR method—application to 2D acoustic scattering problems. Int J Numer Meth Eng. 2023;124(23):5151–82. doi:10.1002/nme.7345.

6. Fu ZJ, Qin QH, Chen W. Hybrid-Trefftz finite element method for heat conduction in nonlinear functionally graded materials. Eng Comput. 2011;28(5):578–99. doi:10.1108/02644401111141028.
7. Mierzwiczak M, Chen W, Fu ZJ. The singular boundary method for steady-state nonlinear heat conduction problem with temperature-dependent thermal conductivity. Int J Heat Mass Transf. 2015;91(3):205–17. doi:10.1016/j.ijheatmasstransfer.2015.07.051.
8. Li T, Gao Y, Han D, Yang F, Yu B. A novel POD reduced-order model based on EDFM for steady-state and transient heat transfer in fractured geothermal reservoir. Int J Heat Mass Transf. 2020;146(1):118783. doi:10.1016/j.ijheatmasstransfer.2019.118783.
9. Simpson RN, Liu Z, Vázquez R, Evans JA. An isogeometric boundary element method for electromagnetic scattering with compatible B-spline discretizations. J Comput Phys. 2018;362:264–89. doi:10.1016/j.jcp.2018.01.025.
10. Lian H, Li X, Qu Y, Du J, Meng Z, Liu J, et al. Bayesian uncertainty analysis for underwater 3D reconstruction with neural radiance fields. Appl Math Model. 2025;138(1):115806. doi:10.1016/j.apm.2024.115806.
11. Fehrle D, Heiberger C, Huber J. Polynomial chaos expansion: efficient evaluation and estimation of computational models. Comput Econ. 2025;65(2):1083–146. doi:10.1007/s10614-024-10772-5.
12. Stfytfkora J, Havelka J. Sparse polynomial chaos expansions for uncertainty quantification in thermal tomography. J Comput Appl Math. 2024;436:115406. doi:10.1016/j.cam.2023.115406.
13. Chen L, Lian H, Dong HW, Yu P, Jiang S, Bordas SPA. Broadband topology optimization of three-dimensional structural-acoustic interaction with reduced order isogeometric FEM/BEM. J Comput Phys. 2024;509:113051. doi:10.1016/j.jcp.2024.113051.
14. Lian H, Zhang Y, Bian N, Qu Y, Li Y, Chen L. Integrating 3DGS novel view synthesis and CFD for modeling bionic robotic fish from multi view imagery. Ocean Eng. 2025;340:122407. doi:10.1016/j.oceaneng.2025.122407.
15. Chen L, Huo R, Lian H, Yu B, Zhang M, Natarajan S, et al. Uncertainty quantification of 3D acoustic shape sensitivities with generalized n th-order perturbation boundary element methods. Comput Meth Appl Mech Eng. 2025;433:117464. doi:10.1016/j.cma.2024.117464.
16. Cruse TA. BIE fracture mechanics analysis: 25 years of developments. Comput Mech. 1996;18(1):1–11. doi:10.1007/s004660050125.
17. Seybert AF, Soenarko B, Rizzo FJ, Shippy DJ. An advanced computational method for radiation and scattering of acoustic waves in three dimensions. J Acoust Soc Am. 1985;77(2):362–8. doi:10.1121/1.391908.
18. Zhao W, Chen L, Chen H, Marburg S. Topology optimization of exterior acoustic-structure interaction systems using the coupled FEM-BEM method. Int J Numer Meth Eng. 2019;119(5):404–31. doi:10.1002/nme.6055.
19. Nagy AP, Abdalla MM, Gürdal Z. Isogeometric sizing and shape optimisation of beam structures. Comput Meth Appl Mech Eng. 2010;199(17–20):1216–30. doi:10.1016/j.cma.2009.12.010.
20. Politis C, Ginnis AI, Kaklis PD, Belibassakis K, Feurer C. An isogeometric BEM for exterior potential-flow problems in the plane. In: 2009 SIAM/ACM Joint Conference on Geometric and Physical Modeling; 2009 Oct 5–8; San Francisco, CA, USA. doi:10.1145/1629255.1629302.
21. Simpson RN, Bordas SPA, Trevelyan J, Rabczuk T. A two-dimensional Isogeometric Boundary Element Method for elastostatic analysis. Comput Meth Appl Mech Eng. 2012;209:87–100. doi:10.1016/j.cma.2011.08.008.
22. Simpson RN, Bordas SPA, Lian H, Trevelyan J. An isogeometric boundary element method for elastostatic analysis: 2D implementation aspects. Comput Struct. 2013;118:2–12. doi:10.1016/j.compstruc.2012.12.021.
23. An Z, Yu T, Bui TQ, Wang C, Trinh NA. Implementation of isogeometric boundary element method for 2-D steady heat transfer analysis. Adv Eng Softw. 2018;116:36–49. doi:10.1016/j.advengsoft.2017.11.008.

24. Li S, Trevelyan J, Zhang W, Wang D. Accelerating isogeometric boundary element analysis for 3-dimensional elastostatics problems through black-box fast multipole method with proper generalized decomposition. Int J Numer Meth Eng. 2018;114(9):975–98. doi:10.1002/nme.5773.
25. Scott MA, Simpson RN, Evans JA, Lipton S, Bordas SPA, Hughes TJR, et al. Isogeometric boundary element analysis using unstructured T-splines. Comput Meth Appl Mech Eng. 2013;254:197–221. doi:10.1016/j.cma.2012.11.001.
26. Nguyen BH, Tran HD, Anitescu C, Zhuang X, Rabczuk T. An isogeometric symmetric Galerkin boundary element method for two-dimensional crack problems. Comput Meth Appl Mech Eng. 2016;306:252–75. doi:10.1016/j.cma.2016.04.002.
27. Peng X, Atroshchenko E, Kerfriden P, Bordas SPA. Isogeometric boundary element methods for three dimensional static fracture and fatigue crack growth. Comput Meth Appl Mech Eng. 2017;316:151–85. doi:10.1016/j.cma.2016.05.038.
28. Chen L, Liu C, Zhao W, Liu L. An isogeometric approach of two dimensional acoustic design sensitivity analysis and topology optimization analysis for absorbing material distribution. Comput Meth Appl Mech Eng. 2018;336:507–32. doi:10.1016/j.cma.2018.03.025.
29. Chen L, Lian H, Liu C, Li Y, Natarajan S. Sensitivity analysis of transverse electric polarized electromagnetic scattering with isogeometric boundary elements accelerated by a fast multipole method. Appl Math Model. 2025;141:115956. doi:10.1016/j.apm.2025.115956.
30. Chen LL, Lian H, Liu Z, Chen HB, Atroshchenko E, Bordas SPA. Structural shape optimization of three dimensional acoustic problems with isogeometric boundary element methods. Comput Meth Appl Mech Eng. 2019;355:926–51. doi:10.1016/j.cma.2019.06.012.
31. Keuchel S, Hagelstein NC, Zaleski O, von Estorff O. Evaluation of hypersingular and nearly singular integrals in the Isogeometric Boundary Element Method for acoustics. Comput Meth Appl Mech Eng. 2017;325:488–504. doi:10.1016/j.cma.2017.07.025.
32. Simpson RN, Scott MA, Taus M, Thomas DC, Lian H. Acoustic isogeometric boundary element analysis. Comput Meth Appl Mech Eng. 2014;269:265–90. doi:10.1016/j.cma.2013.10.026.
33. Chen L, Lu C, Lian H, Liu Z, Zhao W, Li S, et al. Acoustic topology optimization of sound absorbing materials directly from subdivision surfaces with isogeometric boundary element methods. Comput Meth Appl Mech Eng. 2020;362:112806. doi:10.1016/j.cma.2019.112806.
34. Li K, Qian X. Isogeometric analysis and shape optimization via boundary integral. Comput Aided Des. 2011;43(11):1427–37. doi:10.1016/j.cad.2011.08.031.
35. Lian H, Kerfriden P, Bordas SPA. Implementation of regularized isogeometric boundary element methods for gradient-based shape optimization in two-dimensional linear elasticity. Int J Numer Meth Eng. 2016;106(12):972–1017. doi:10.1002/nme.5149.
36. Lian H, Kerfriden P, Bordas SPA. Shape optimization directly from CAD: an isogeometric boundary element approach using T-splines. Comput Meth Appl Mech Eng. 2017;317:1–41. doi:10.1016/j.cma.2016.11.012.
37. Lin X, Zheng W, Zhang F, Chen H. Uncertainty quantification and robust shape optimization of acoustic structures based on IGA BEM and polynomial chaos expansion. Eng Anal Bound Elem. 2024;165:105770. doi:10.1016/j.enganabound.2024.105770.
38. Liu C, Chen L, Zhao W, Chen H. Shape optimization of sound barrier using an isogeometric fast multipole boundary element method in two dimensions. Eng Anal Bound Elem. 2017;85:142–57. doi:10.1016/j.enganabound.2017.09.009.
39. Son J, Du Y. An efficient polynomial chaos expansion method for uncertainty quantification in dynamic systems. Appl Mech. 2021;2(3):460–81. doi:10.3390/applmech2030026.
40. Novák L, Sharma H, Shields MD. Physics-informed polynomial chaos expansions. J Comput Phys. 2024;506:112926. doi:10.1016/j.jcp.2024.112926.

41. Gao XW. The radial integration method for evaluation of domain integrals with boundary-only discretization. Eng Anal Bound Elem. 2002;26(10):905–16. doi:10.1016/S0955-7997(02)00039-5.
42. Borden MJ, Scott MA, Evans JA, Hughes TJR. Isogeometric finite element data structures based on Bézier extraction of NURBS. Int J Numer Meth Eng. 2011;87(1–5):15–47. doi:10.1002/nme.2968.
43. Chen LL, Zhang Y, Lian H, Atroshchenko E, Ding C, Bordas SPA. Seamless integration of computer-aided geometric modeling and acoustic simulation: isogeometric boundary element methods based on Catmull-Clark subdivision surfaces. Adv Eng Softw. 2020;149:102879. doi:10.1016/j.advengsoft.2020.102879.
44. Gao XW, Peng HF. Theory and program of advanced boundary element method. Beijing, China: Science Press; 2015. (In Chinese).
45. Qu XY, Dong CY, Bai Y, Gong YP. Isogeometric boundary element method for calculating effective property of steady state thermal conduction in 2D heterogeneities with a homogeneous interphase. J Comput Appl Math. 2018;343(1):124–38. doi:10.1016/j.cam.2018.04.053.
46. Gong Y, Trevelyan J, Hattori G, Dong C. Hybrid nearly singular integration for isogeometric boundary element analysis of coatings and other thin 2D structures. Comput Meth Appl Mech Eng. 2019;346:642–73. doi:10.1016/j.cma.2018.12.019.
47. Gao XW, Davies TG. Boundary element programming in mechanics. Cambridge, UK: Cambridge University Press; 2002.
48. Chen L, Liu C, Lian H, Gu W. Electromagnetic scattering sensitivity analysis for perfectly conducting objects in TM polarization with isogeometric BEM. Eng Anal Bound Elem. 2025;172:106126. doi:10.1016/j.enganabound.2025.106126.
49. Wang L, Guo C, Xu F, Xiao H. Hybrid uncertainty propagation for mechanical dynamics problems via polynomial chaos expansion and Legendre interval inclusion function. Mech Syst Signal Process. 2025;223:111826. doi:10.1016/j.ymssp.2024.111826.